ELECTRICAL PROPERTIES OF ZnO GROWN BY METALORGANIC VAPOUR PHASE EPITAXY

by

Dichen Li
B.Sc., University of Science and Technology of China, 2008

THESIS SUBMITTED IN PARTIAL FULFILLMENT OF
THE REQUIREMENTS FOR THE DEGREE OF

MASTER OF SCIENCE

In the Department of Physics

SIMON FRASER UNIVERSITY

Summer 2011

APPROVAL

Name:	**Dichen Li**
Degree:	**Master of Science**
Title of Thesis:	**Electrical Properties of ZnO Grown by Metalorganic Vapour Phase Epitaxy**

Examining Committee:

Chair: **Dr. J. Steven Dodge**

Supervisor
Dr. Simon Watkins

Supervisor
Dr. Karen Kavanagh

Supervisor
Dr. Patricia Mooney

Internal Examiner
Dr. Gary Leach

Date Defended/Approved:

ABSTRACT

ZnO is a wide band gap semiconductor which is a good candidate for the next generation of visible and ultraviolet optoelectronic devices. The electrical properties of thin film ZnO grown on sapphire by metalorganic vapour phase epitaxy (MOVPE) were investigated in this thesis. Hall measurements were performed to determine the electrical properties of the ZnO layers. Films were found to be *n*-type in all cases with residual carrier densities in the range 5×10^{17} to 2×10^{18} cm^{-3}. The addition of In dopant did not result in a significant increase in *n*-doping despite a large In concentration determined by secondary ion mass spectrometry and low temperature photoluminescence spectroscopy. Temperature dependent Hall measurements showed carrier freeze-out with an activation energy of ~30 meV which is attributed to native donors. No significant change in activation energy was observed for In doping, consistent with poor activation of the In impurities. These data indicate that under the present conditions, In primarily incorporates as an electrically inactive phase. Thermally deposited Al Ohmic contacts were developed, having a sheet resistance of $<10^{-5}\ \Omega\ \mathrm{cm}^2$. Devices were fabricated with top side Al Ohmic contacts and Au rectifying contacts on ZnO epilayers. The effect of oxygen plasma and hydrogen peroxide wet treatments were studied by *I*-*V* and *C*-*V* measurements. Au-ZnO devices showed rectifying behaviour but with significant leakage and high ideality factors compared with bulk substrate material. Some improvement was observed for devices treated with oxygen plasma treatment.

ACKNOWLEDGEMENTS

I would like to thank my mother, my grandmother, all my friends and my supervisor

Simon Watkins

TABLE OF CONTENTS

LIST OF FIGURES

LIST OF TABLES

1: INTRODUCTION

ZnO is a wide band gap semiconductor with a large exciton binding energy of 60 meV at room temperature making it important for ultra-violet optical devices. [1] ZnO is very easy to etch in several common acids or alkalis, making it suitable for small-size device fabrication. [2] In addition, ZnO has a similar crystal structure and lattice constant to GaN, so that it can be used as a substrate for GaN thin films. All these properties, as well as resistance to high energy radiation, lower cost and less toxic material, have resulted in an extraordinary level of interest from researchers over the past decade.

However, some problems need to be solved before ZnO can be used to make optoelectronic devices. Growth of good crystal quality ZnO on sapphire substrates, which is highly desirable for low cost light emitting diodes, is very challenging. Also, a reproducible method for making *p*-type ZnO still has not been reported. It is still uncertain whether it is intrinsic defects such as Zn interstitials and oxygen vacancies or hydrogen impurities which are responsible for making as-grown *n*-type ZnO. [2] Even for the case of intentional *n*-doping, it is not clear whether the doping effect is caused by substitutional point defects, or by complexes with native defects. Also, despite the fact that rectifying contacts on ZnO are very important for ZnO device applications, [2] up to now there are still limited reports for rectifying contacts on thin film ZnO, especially for growth by metalorganic vapour phase epitaxy (MOVPE). This thesis will focus on the electrical properties of ZnO grown on sapphire and Si substrates by MOVPE and on the formation of metal-semiconductor contacts on MOVPE–grown ZnO. Chapters 2 and 3 will introduce the semiconductor theory and basic experimental methods including the device fabrication methods. Chapter 4 will investigate the structural and electrical properties of ZnO, especially for In and Al doping in ZnO and the effects of substrate annealing. Also, data from temperature dependent Hall measurements will be presented and discussed. Chapter 5 will show the results from current-voltage and capacitance-voltage measurements for Au rectifying contacts on ZnO. A model to describe the trends of these measurements on device area will be provided in this chapter.

2: THEORY

This chapter will introduce and explain the theory and background for performing the experiments during the study of ZnO material. In this chapter, the theory of metal-semiconductor contacts will be presented. Hall effect measurements and temperature dependent Hall effect will be introduced.

2.1 Metal-semiconductor contact

It is very important to understand the energy band structure and electrical behavior of rectifying and Ohmic contacts for fabrication of devices on ZnO. In this chapter, an overview of energy bands of metal-semiconductor junctions will be discussed, as well as the theory behind current-voltage (*I*-*V*) and capacitance-voltage (*C*-*V*) characterization.

A Schottky contact is an idealized metal-semiconductor junction with rectifying current-voltage characteristics and is important for certain device applications. An Ohmic contact is a metal-semiconductor junction having linear current-voltage characteristics. Ohmic contacts are very important because they link semiconductor devices with the outside world by carrying current into and out of devices with low resistance. [2] In this section, we will study the physics of metal semiconductor contacts using a band diagram picture, and then elaborate on the *I*-*V* and *C*-*V* characterization of Ohmic and rectifying contacts.

2.1.1 Schottky barrier model of rectifying contacts

Fig 2.1 illustrates the energy band diagram before metal-semiconductor contact. Since our sample is *n*-type ZnO, we mainly focus on *n*-type semiconductors. ϕ_m is the metal work function, which is the energy needed to move an electron out of a particular metal into the vacuum. Typical values of ϕ_m for Al and Au are 4.3 eV and 4.8 eV respectively. ϕ_s is the semiconductor work function, defined as the energy difference between the vacuum level potential and the Fermi level of a particular semiconductor. χ is the electron affinity which is defined as the energy difference between the vacuum energy and the conduction band.

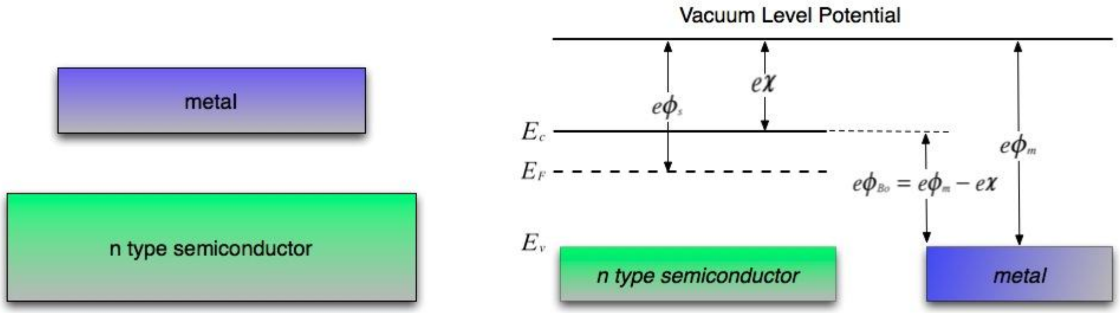

Figure 2.1 Band diagram of metal and semiconductor before contact.

The potential energy needed to move an electron from the metal to the semiconductor can be divided into two parts: the electron is first taken out of the metal to the vacuum level; then transported from vacuum level into the semiconductor. So ideally, the total energy required to move the electron from the metal to the semiconductor, also defined as the Schottky barrier height, is just the difference between the work function of the metal and the electron affinity of the semiconductor. The Schottky barrier height ϕ_{B0} is computed as: [3]

$$\phi_{B0} = \phi_m - \chi \,. \tag{2.1}$$

When the semiconductor and metal are joined, there exists an energy difference between the Fermi levels of the two materials. Usually, the Fermi level of the n-type semiconductor is higher than that of metal, making the electrons flow from the semiconductor into the lower energy level in the metal. This process will not stop until the Fermi energy levels in these two materials reach equilibrium. Similar to a one sided p-n junction, in the n-type semiconductor, a depletion region or space charge region W is formed near the junction resulting in a bending of the energy band due to the charge layer which is established in the depletion region, which can be seen from Fig 2.2.

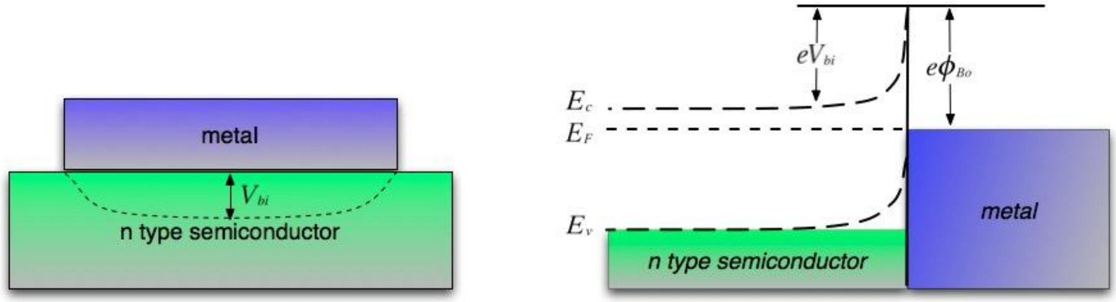

Figure 2.2 Band diagram of metal and semiconductor when contacted to each other.

From the semiconductor side, to go through the junction, electrons also need to cross over the barrier created by the space charge region, this barrier V_{bi} is called the built-in potential barrier, given by [3]:

$$V_{bi} = \phi_m - \phi_s \,. \tag{2.2}$$

It is worth pointing out that the Schottky barrier height is a fixed value determined by the kind of metal and semiconductor that we choose. The Schottky barrier height will not change as the voltage across the diode. In contrast, the applied voltage does change the magnitude of the barrier height across the space charge region in the semiconductor which is e(V_R+V_{bi}). This difference is very important for understanding Schottky contact electrical behaviour.

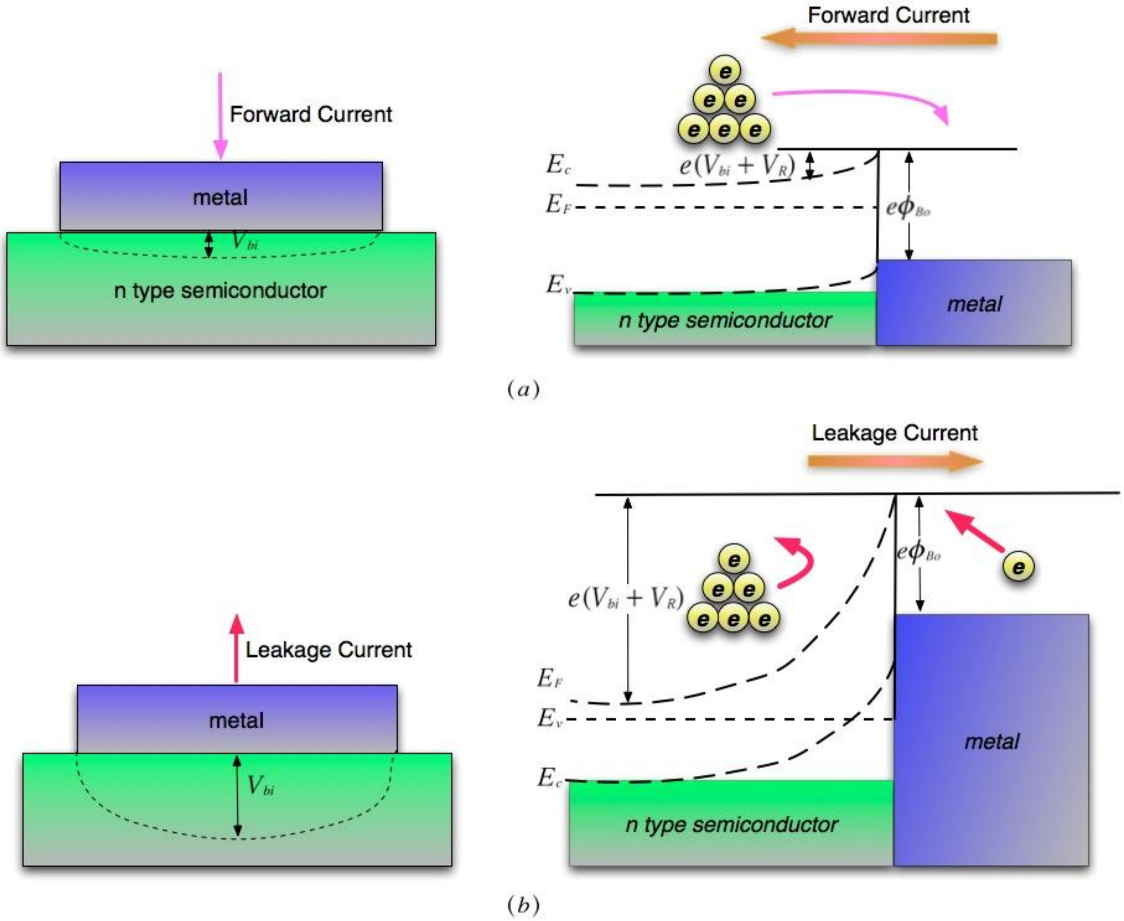

Figure 2.3 Schottky diode with energy band diagram (a) under forward bias (b) under reverse bias.

As illustrated in Fig 2.3(a), if a positive voltage is applied to the metal with respect to the semiconductor, V_R is negative so the barrier height across the space charge region decreases, while the Schottky barrier height remains constant. In this situation, more and more electrons can cross over the barrier to reach to the metal since the barrier height decreases. The shrinkage of the depletion width will also make it easier for electrons to cross the barrier, just as in the case of the p-n junction. This results in a rapid increase of forward current with voltage observed in the I-V measurements. On the other hand, if we apply a positive voltage to the semiconductor with respect to the metal, it will increase the barrier height across the space charge region, although the Schottky barrier height remains constant, and the depletion width also increases. As is shown in Fig 2.3 (b), in this condition, only a few electrons can get over such a relatively large barrier, flowing from the semiconductor into the metal.

2.1.2 Current-voltage characteristics

The current-voltage characteristics of the ideal Schottky barrier junction are similar to the rectifying behaviour of a p-n junction. In forward bias, the current depends on how many majority carrier electrons can get over the built-in potential barrier from the semiconductor to the metal side. This process can be described using thermionic emission theory. [3]

The net current density should be the combination of the current density from the semiconductor to metal, $J_{s\to m}$ and the current density in the opposite direction, $J_{m\to s}$. The net current density is

$$J = J_{s\to m} - J_{m\to s}\,. \tag{2.3}$$

The Maxwell-Boltzmann approximation can be used to calculate the concentration of the electrons that have enough energy to cross the barrier. [3] This can be shown to have the following simple form:

$$J = J_{sT}\left[exp\left(\frac{eV_a}{kT}\right) - 1\right], \tag{2.4}$$

where $J_{sT} = A^*T^2exp\left(\frac{-e\phi_{Bn}}{kT}\right)$ is the reverse-saturation current density and $A^* = \frac{4\pi em_n^*}{h^3}$ is called the effective Richardson constant for thermionic emission. ϕ_{B0} is the Schottky barrier height. Although the current-voltage relationship in a p-n junction and a Schottky barrier diode have a very similar form, the current mechanisms are very different in these two devices. The current in a p-n junction is determined by the diffusion of the minority carriers, while thermal emission of majority carriers over a potential barrier determines the current in Schottky diode.

2.1.3 Capacitance-Voltage characteristics

Capacitance voltage (*C*-*V*) measurements can be used to determine the donor concentration in the semiconductor. This concentration can also be compared with the free electron concentration determined from Hall measurements.

As in a p-n junction, a Schottky diode also forms a depletion region, but the depletion region of a Schottky contact is only located in the semiconductor side. In the theory of the p-n junction, Poisson's equation is used for a one-dimensional derivation. [3]

$$\frac{d^2\phi(x)}{dx^2} = \frac{-\rho(x)}{\varepsilon_s} = -\frac{dE(x)}{dx}\ . \tag{2.5}$$

First we consider the case of an abrupt p-n junction. Assuming that the electric field at both edges of the depletion area is zero, the space charge depletion width of the p-n junction can be approached as:

$$W = x_p + x_n = \left\{\frac{2\varepsilon_s(V_{bi} + V_R)}{e}\left[\frac{N_a + N_d}{N_aN_d}\right]\right\}^{\frac{1}{2}}\ . \tag{2.6}$$

A metal-*n*-type semiconductor junction is conceptually similar to a p-n junction with a very high hole density. This means that we can borrow equation 2.6 for the case $N_A >> N_D$. In this case, equation 2.6 reduces to:

$$W = x_n = \left[\frac{2\varepsilon_s(V_{bi} + V_R)}{eN_d}\right]^{1/2} , \tag{2.7}$$

where V_R is the magnitude of the applied reverse-bias voltage. For a Au Schottky contact on a ZnO sample with electron concentration 1×10^{18} cm^{-3}, the depletion width is 20 nm.

The junction capacitance is given by:

$$C = \frac{dQ}{dV_R} = \frac{eN_d A dx_n}{dV_R} = A\left[\frac{e\varepsilon_s N_d}{2(V_{bi} + V_R)}\right]^{1/2} . \tag{2.8}$$

This equation can be rewritten as:

$$\left(\frac{1}{C}\right)^2 = \frac{2(V_{bi} + V_R)}{e\varepsilon_s A^2 N_d} . \tag{2.9}$$

From equation 2.9, there exists a linear relationship between the applied voltage and the reciprocal of the square of the capacitance. The donor concentration N_d can be determined from the slope of the $1/C^2$ vs. V_R data, while the built-in potential can be obtained from the intercept on the *x*-axis. In addition, we can determine the Schottky barrier height from the V_{bi} that we get from *C*-*V* measurements. Considering equation 2.1 and 2.2, we find that there is only a slight difference between the Schottky barrier height and built-in potential:

$$\phi_{B0} = V_{bi} + \phi_n , \tag{2.10}$$

where ϕ_n is the difference in energy between the bottom of the conduction band and the Fermi energy.

2.1.4 Ohmic contacts

Metal-semiconductor junctions can also form Ohmic contacts. The type of contact, Schottky barrier or Ohmic, depends mostly on the work function of the metal and semiconductor.

We still take an *n*-type semiconductor as an example. If the work function of the semiconductor ϕ_s is greater than the work function of the metal ϕ_m, as shown in Fig. 2.4(a), the Fermi energy of the semiconductor is lower than that of the metal, resulting in a transfer of electrons from the metal to semiconductor until equilibrium is reached. Fig. 2.4(b) illustrates the band diagram of an Ohmic contact. The effective barrier height for electrons flowing from the metal to semiconductor is very small for electrons to overcome. Compared with the Schottky contact formation process, the majority carrier electrons flow from the metal into the semiconductor, making it more *n* type, thus there is no space charge region in the semiconductor. No matter how the voltage is applied across the junction, the barrier height does not change. Electrons only need to get over a small barrier to transfer from the metal to the semiconductor.

Tunneling barriers are also frequently used to form Ohmic contacts. [4] From equation 2.7, we can see the space charge width in a rectifying metal-semiconductor contact is inversely proportional to the square root of the carrier concentration. So if the concentration is too high, then the space charge region is very thin. That can increase the possibility of tunneling, making it an Ohmic contact. Therefore it is very difficult to make Schottky contacts on a semiconductor with a high carrier concentration.

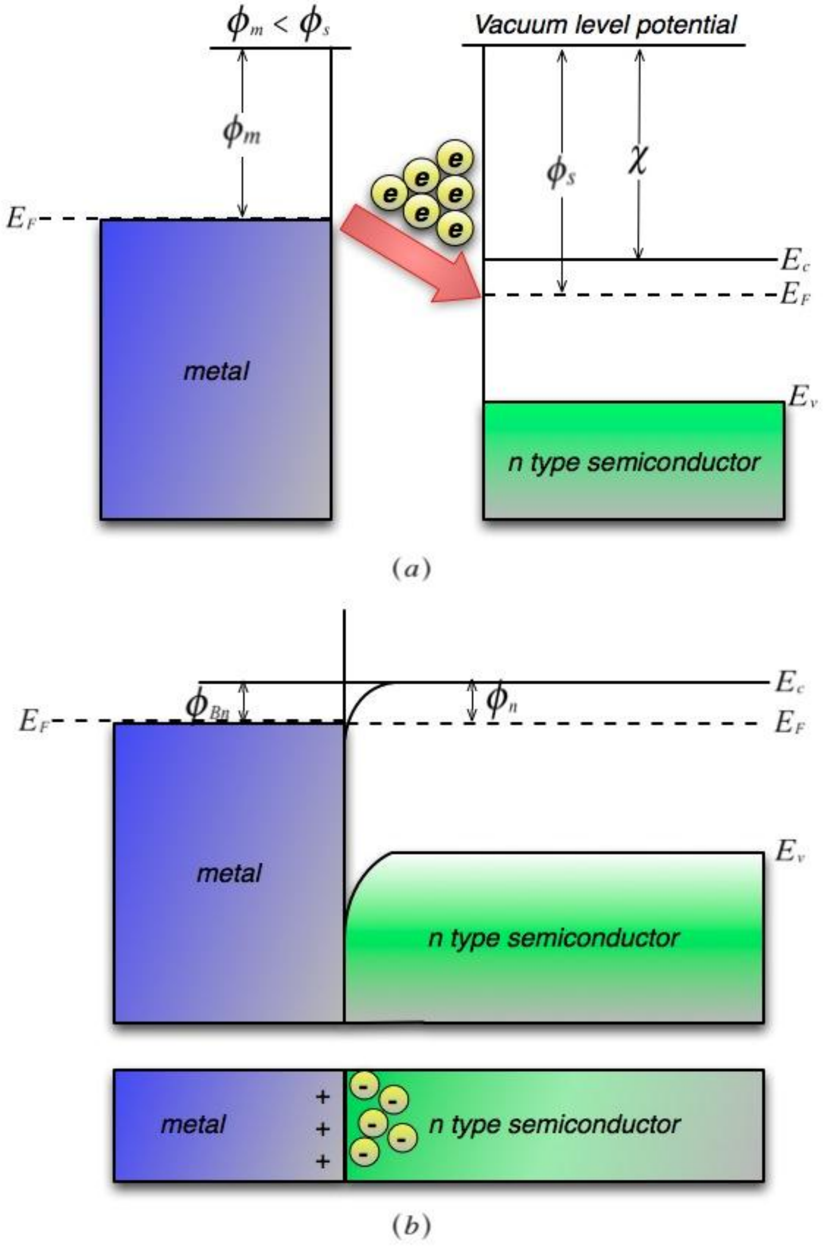

Figure 2.4 (a) Ohmic contact for *n* type semiconductor before contact; (b) the equilibrium band diagram for the junction.

2.1.5 Transmission line measurements

Since Ohmic contacts are critical in circuit design, it is important to make low resistance Ohmic contacts for particular semiconductor materials.

To determine the quality of an Ohmic contact, we define the specific contact resistance.

$$\rho_c = \left.\frac{\partial V}{\partial J}\right|_{V=0} . \tag{2.11}$$

We want ρ_c to be small to make a good Ohmic contact. Generally, the specific contact resistance is $\rho_c < 10^{-6}$ $\Omega\cdot\mathrm{cm}^2$ for a good Ohmic contact. [5]

As is shown in Fig 2.5, when we measure the total resistance between two metal contacts, there are three contributions to the measured resistance: (1) metal resistance R_m (2) contact resistance R_c , (3) semiconductor resistance R_S. The total resistance is: [5]

$$R = 2R_m + 2R_c + R_s . \tag{2.12}$$

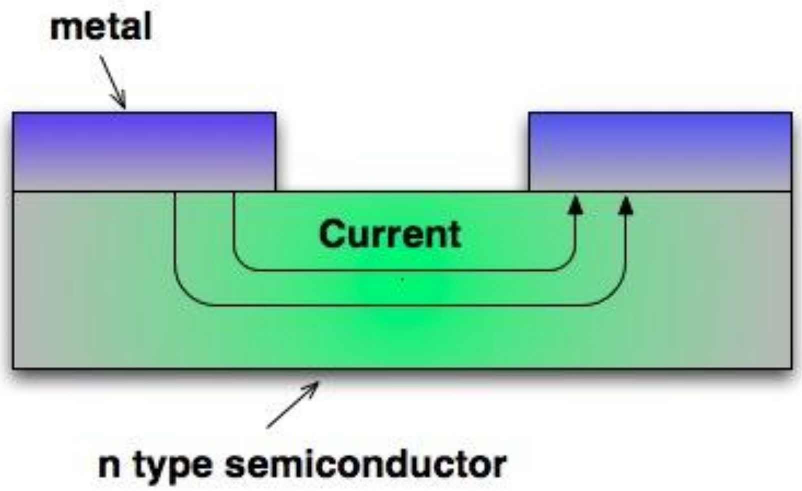

Figure 2.5 Schematic diagram showing current flow between metal contacts adapted from [5].

Since most metals are highly conductive, R_m can usually be neglected. The dominant contributions are usually due to the semiconductor and the contact resistance. Current flow analysis reveals current crowding effects, [6] which means that the current lines only flow through part of the metal contact area. To find ρ_c, we must consider more details about the current flow into and out of the metal contact.

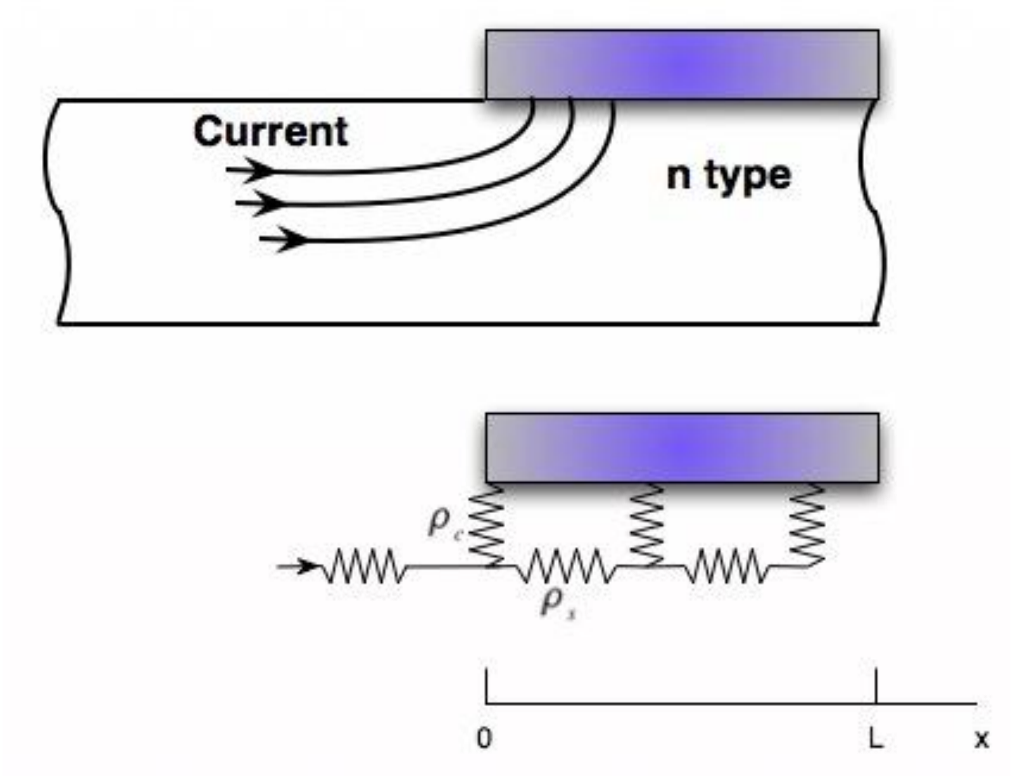

Figure 2.6 Schematic of current flowing from semiconductor into metal contact and equivalent circuit with the current choosing the path of least resistance adapted from [5].

The transmission line model (TLM) was provided by Murrmann and Widmann to find the contact resistance at a semiconductor-metal junction. [7] This model is now widely used in semiconductor physics and engineering. As shown in Fig 2.6, when current flows from a semiconductor into metal, it chooses the path of least resistance. [5] According to H.H.Berger's analysis, [8] the potential distribution under the metal contact is given below: [5]

$$V(x) = \frac{I\sqrt{\rho_c \rho_s}\cosh[(L-x)/L_T]}{Z\sinh(L/L_T)}\,, \tag{2.13}$$

where L is the contact length, Z is the contact width, I is the current flowing into the contact, ρ_c is the specific contact resistance, ρ_s is sheet resistance of the semiconductor.

From equation 2.13, it follows that the voltage is the highest at the edge of the contact (x=0) and decreases rapidly with distance. The voltage can be neglected over a particular distance, which is defined as the transfer length:

$$L_T = \sqrt{\frac{\rho_c}{\rho_s}}\,. \tag{2.14}$$

The transfer length can be thought of as a distance within which, from the edge of the contact, most of current transfers from the metal into the semiconductor or from the semiconductor into the metal. Typical transfer lengths are less than 1 micron and in most cases, the transfer length is much smaller than the contact length. [5] This means most of the contact area is "inactive".

Now we may consider the contact resistance. From equation 2.13 we have:

$$R = \frac{V}{I} = \frac{\rho_c}{L_T Z} coth\left(\frac{L}{L_T}\right). \tag{2.15}$$

Equation 2.15 is just an approximation of the contact resistance, because we just suppose that all the current flows along one dimension i.e. there is no spreading perpendicular to the line between the contacts. Figure 2.7a shows the typical geometry used in this work. In order to confine the current, we etched a mesa on the ZnO layer down to the sapphire substrate. We only make metal contact on these mesas so that the current is confined to transfer along the ZnO mesa, since sapphire is an insulator.

For $L \leq 0.5L_T$, $\coth(L/L_T) \approx L_T/L$, and therefore:

$$R_c \approx \frac{\rho_c}{LZ}\,. \tag{2.16}$$

For $L \geq 1.5L_T$, $\coth(L/L_T) \approx 1$, and therefore we get

$$R_c \approx \frac{\rho_c}{L_T Z}\,. \tag{2.17}$$

In the second condition, which includes most cases, the effective contact area is $A = L_T Z$. So the effective contact area is much smaller than the real contact area. [5] Next, we consider our TLM model illustrated in Fig 2.7. The metal contact was deposited on the semiconductor with a particular variable spacing d_i. The resistance was then measured between adjacent pairs of metal contacts with increasing separation. Then we plot the measured resistances as a function of spacing.

For contacts with $L \geq 1.5L_T$, the total resistance between any two contacts should be [5]

$$R_T = \frac{\rho_s d}{Z} + 2R_c \approx \frac{\rho_s}{Z}(d + 2L_T)\,. \tag{2.18}$$

The slope of this line gives the sheet resistance of the semiconductor by multiplying by the width Z of the contact. Secondly, the intercept on the R-axis gives $2R_c$. We can obtain the transfer length L_T from the intercept on the d-axis. We have assumed that $L \geq 1.5L_T$, so this transfer length can also help double-check this preliminary assumption. Moreover, from equation 2.14, we can calculate the specific contact resistance, which is the more important parameter, as it is independent of the contact area.

Care must be taken in obtaining the contact resistance. For example, a small change of the slope can lead to a large relative change in the *d*-axis intercept. That means that the transfer length we get from the intercept at R_T=0 may have large uncertainties.

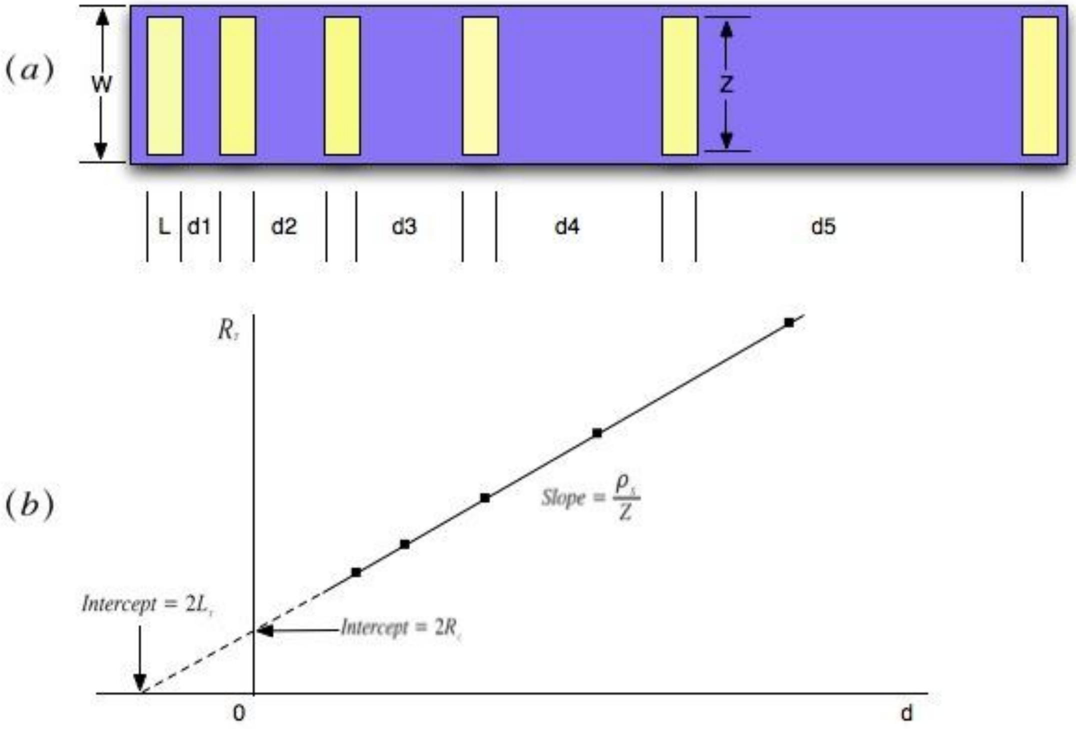

Figure 2.7 Transfer length method (a) diagram of test structure and (b) plot of total resistance versus contact spacing adapted from [5]

2.2 Hall effect

Hall effect measurements are widely used in semiconductor technology to determine the carrier concentration and mobility of semiconductor materials. In this section, the basic principle of the Hall effect and van der Pauw theory will be introduced.

2.2.1 Hall effect theory

We assume that an electron travels through a sample, with a velocity v_x. Under a magnetic field in the z direction, the electron experiences a Lorentz force perpendicular to the current flow. This Lorentz force results in an accumulation of static positive and negative charges on opposite sides of the sample resulting in a transverse voltage known as the Hall voltage.

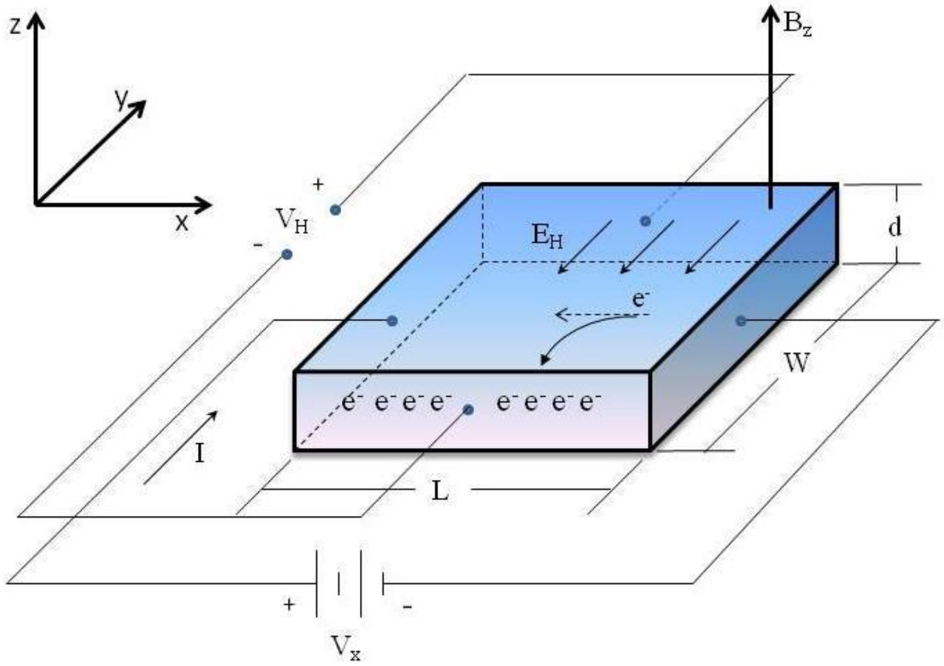

Figure 2.8 Geometry for measuring Hall effect adapted from [3].

Fig 2.8 shows this process. Once the equilibrium is reached, Lorentz force must balance the electric force induced by the static charges:

$$\vec{F}= e\left[\vec{E} + \vec{v} \times \vec{B}\right] = 0\,. \tag{2.18}$$

If we construct the frame as shown in Fig 2.8, equation 2.18 can be written in components:

$$eE_y = ev_xB_z\,, \tag{2.19}$$

where v_x is the drift velocity of the electrons, which can be related to the current density by:

$$J_x = \frac{I}{Wd} = \frac{Wdv_xne}{Wd} = v_xne\,, \tag{2.20}$$

where E_y is an induced electric field and is called the Hall field E_H. This electric field can be measured by measuring the voltage across the sample, which is defined as the Hall voltage.

$$V_H = E_HW\,. \tag{2.21}$$

We define the Hall coefficient R_H as:

$$R_H = \frac{E_y}{B_zj_x} = \frac{V_Hd}{IB_z}\,. \tag{2.22}$$

Equation 2.22 can be obtained by measuring the applied magnetic field, the current, the Hall voltage, and knowledge of the geometry of the sample. Plugging equation 2.19 and 2.20 into 2.22, the Hall coefficient can also be written as:

$$R_H = \frac{1}{ne}\,. \tag{2.23}$$

From equation 2.23, the carrier concentration can be computed once the Hall coefficient is known.

2.2.2 van der Pauw theory

It is very inconvenient to measure the Hall effect following the traditional bar geometry described above for the reason that the shape of the sample is rather difficult to make. van der Pauw provided a method in 1958 and solved the problem successfully for a thin layer for arbitrary shape with four point-like contacts along the periphery. [9] This method involves only 4 contacts, and is now widely used in determining the electrical properties such as carrier concentration and Hall mobility in semiconductors.

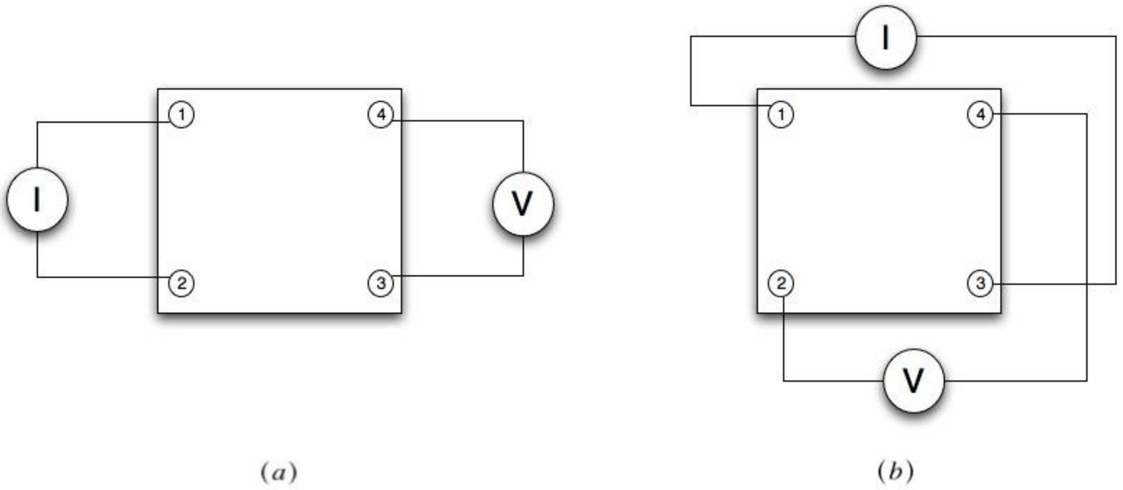

.Figure 2.9 Contact for (a) resistivity measurement (b) Hall measurement.

The resistivity is measured at zero magnetic field as shown in Fig 2.9 (a) for one of two possible configurations. We define the resistance $R_{mn,op} = V_{mn}/I_{op}$. I_{op} as the current flow from point O to point P and $V_{mn} = V_m - V_n$ where m,n,o,p are integer labels for the contacts shown in Fig. 2.9. Van der Pauw showed that the resistivity of the sample can be expressed as:

$$\rho = \frac{\pi d}{ln2} \cdot \left[\frac{R_{21,34} + R_{32,41}}{2}\right] f \,, \tag{2.24}$$

where *f* is a correction factor which should equal 1 for a square or circular sample. This correction factor *f* is determined by a ratio $Q = R_{21,34}/R_{32,41}$. The relationship between *f* and Q result in the following: [10]

$$\frac{Q-1}{Q+1} = \frac{f}{ln2} arccosh\left[\frac{1}{2} exp\left(\frac{ln2}{f}\right)\right] . \tag{2.25}$$

This equation is solved numerically to obtain *f*. To find the resistivity, we calculate Q from the measurement, and then determine *f* from the equation 2.25 and then find the resistivity from equation 2.24. It is worth pointing out that, *f* is just a geometric correction factor and has nothing to do with resistivity of the material. [10] However, the presence of a large *f* factor can indicate a problem with the sample such as non-uniform carrier concentration or mobility.

To increase the accuracy, additional measurements were taken by using multiple contact arrangements and changing the direction of the current. [11] The resistivity can then be expressed as:

$$\rho = \frac{\pi d}{8ln2} \cdot \left[\left(R_{34,12} - R_{34,21} + R_{23,41} - R_{23,14}\right) f_A + \left(R_{12,34} - R_{12,43} + R_{41,23} - R_{41,32}\right) f_B\right] , \tag{2.26}$$

where f_A and f_B are calculated from the experimental data and Q_A and Q_B are given by:

$$Q_A = \frac{R_{34,12} - R_{34,21}}{R_{23,41} - R_{23,14}} \ and \ Q_B = \frac{R_{12,34} - R_{12,43}}{R_{41,23} - R_{41,32}} \,. \tag{2.27}$$

The resistivity was calculated using equation 2.26. To obtain the Hall coefficient, the magnetic field needs to be applied perpendicular to the sample surface. According to van der Pauw theory, the Hall coefficient can be written as:

$$R_H = \frac{d}{B}\left(\frac{R_{13,42} + R_{42,31}}{2}\right) , \tag{2.28}$$

where the resistance values are defined in Fig 2.9 (b).

Similar to the resistivity measurements, the Hall coefficient measurements are obtained by averaging over all contacts and directions of the magnetic field.

$$R_{H1} = \left(\frac{d}{4B}\right)\left[R_{31,42} - R_{13,42} + R_{42,13} - R_{24,13}\right], \tag{2.29}$$

$$R_{H2} = \left(\frac{d}{4B}\right)\left[R_{13,42} - R_{31,42} + R_{24,13} - R_{42,13}\right], \tag{2.30}$$

where R_{H1} and R_{H2} are the Hall coefficients measured using opposite directions of the magnetic field. R_H can be obtained by taking the average over R_{H1} and R_{H2}.

2.2.3 Temperature dependent Hall measurements

Temperature dependent Hall measurements were also an important part of this project. Information such as the donor activation energy can be extracted from temperature dependent Hall measurements.

Impurities in semiconductors can change the electrical properties of semiconductors. We take *n*-type ZnO for example. Consider adding a low concentration of group III dopant atoms such as Al, In or Ga, which have three electrons in their outer shells. These group

III elements will substitute for Zn atoms, which have only two electrons in their outer shells. Only two of these group III valence electrons will form covalent bonds with oxygen atoms, leaving an extra electron which is weakly bonded to the extra charge of the donor ion. This electron can be easily promoted to the conduction band at higher temperature and the energy needed to elevate this electron into conduction band is significantly less than the covalent bonding energy. Fig 2.10 (a) shows the donor energy level relative to the conduction band minimum. E_d is the binding energy of the donor electron. At high temperatures, electrons in donor states will jump to the conduction band leaving fixed positively charged ions. If the temperature decreases, the electrons in the conduction band will be trapped by these shallow donor levels, resulting in a drop in the free carrier density called freeze-out. Freeze-out can only occur for so-called non-degenerate doping, which occurs when the individual dopant atoms are at low concentrations such that the wave functions of the donors do not overlap (Fig. 2.10a).

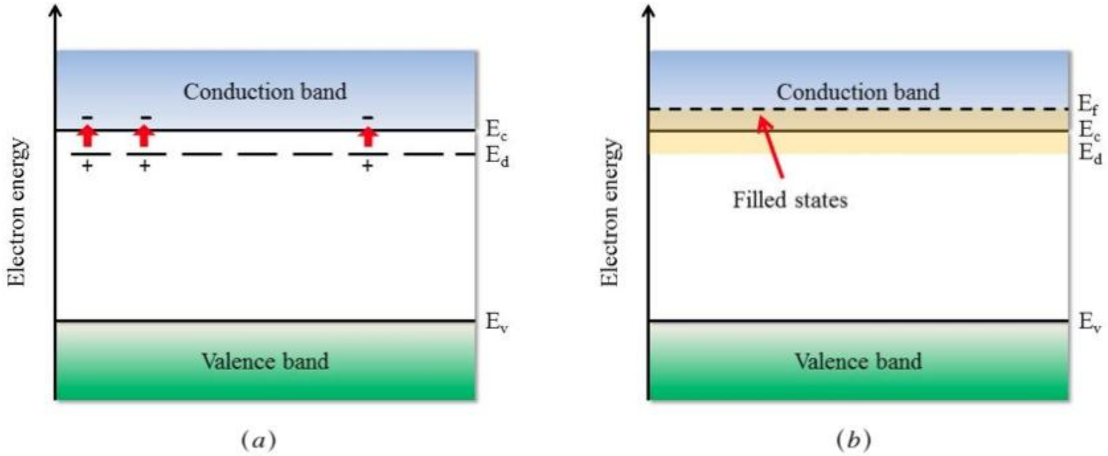

Figure 2.10 The energy band diagram for (a) donor state of non-degenerate and (b) degenerate *n*-type semiconductors.

At high impurity concentrations, the interaction between the impurities should be taken into consideration. In this case, the single donor energy levels will split and form a band. (Fig 2.10 (b)) If the doping concentration further increases, this band will become wider and finally overlap the bottom of the conduction band. If the donor concentration is very high, the Fermi level will shift up into the conduction band. This kind of semiconductor is called a degenerate *n*-type semiconductor. Under these conditions, freeze-out is not possible because the band of donor states forms a continuum which merges with the conduction band.

We consider the case of an *n*-type semiconductor. The form of the Fermi-Dirac function for electrons can be written as: [3]

$$f(E) = \frac{1}{1 + \frac{1}{g} exp\left(\frac{E_d - E_f}{kT}\right)}\ , \tag{2.31}$$

where g is the spin degeneracy factor, g=2 for electrons, and E_d is the ionization energy of the donor level. The electron concentration occupying the electron donor levels is:

$$n_d = \frac{N_d}{1 + \frac{1}{g} exp\left(\frac{E_d - E_f}{kT}\right)}\ , \tag{2.32}$$

where N_d is concentration of donor atoms. The ionized donor concentration can be expressed as:

$$N_d^+ = N_d - n_d = \frac{N_d}{1 + gexp\left(\frac{E_f - E_d}{kT}\right)} = \frac{N_d}{1 + g\frac{n}{N_c} exp\left(\frac{\Delta E_d}{kT}\right)}\ , \tag{2.33}$$

where $N_c = 2\left(\frac{2\pi m_n^* kT}{h^2}\right)^{3/2}$ is the effective density of states function in the conduction band. $\Delta E_d = E_c - E_d$ is the activation donor energy that equals the difference between the conduction band energy minimum and the donor energy level, and n is the electron concentration in the conduction band. The charge neutrality condition, which requires that the positive charge should be equal to the negative charge in the neutral part of the semiconductor, can be written as:

$$n + N_a^- = p + N_d^+ \, , \tag{2.34}$$

where p is the hole concentration in the valence band and N_a^- is the concentration of ionized negatively charged acceptors. Since our semiconductor is n type, the hole concentration in the valence band can be neglected and $N_a^- = N_a - p \approx N_a$. In this case, equation 2.34 can be simply written as:

$$n + N_a = N_d^+ \, . \tag{2.35}$$

Plugging 2.33 into 2.35 we can rewrite the charge balance equation as:

$$n + N_a = \frac{N_d}{1 + \frac{n}{\phi_d}} \, , \tag{2.36}$$

where $\phi_d = \frac{N_c' T^{3/2}}{g} exp\left(\frac{\Delta E_d}{kT}\right)$ and N_c' is the effective density of states function at T=1K, N_d, g and ΔE_d represent the donor concentration, degeneracy factor and donor activation energy. From equation 2.36, we can see that n is a function of temperature and N_a, N_d and ΔE_d can be extracted by fitting the n versus T plot, which can be obtained from temperature dependent Hall measurements.

3: EXPERIMENTAL METHODS

This chapter mainly provides an introduction to the experimental methods used for Schottky device fabrication and the preparation for Hall measurement samples. The Schottky device fabrication was performed using photolithography.

3.1 Photolithography

Photolithography is a process to optically transfer a device pattern onto a substrate. Photolithography must be performed in an ultraclean environment because even a little contamination will result in defects in the photoresist coating. If the defects appear on more than 10% of the chip surface during each photolithography step, it will cause more than 50% of the chips to be useless. [12] Since the dimensions of the devices are in the micron range, and the devices are sensitive to particles in the air, all the processing is performed in a cleanroom. The specific details about each photolithography step will be discussed later in this section.

3.1.1 Mask design

A photomask is used to define a particular pattern which we want to “print” onto the semiconductor wafer. The mask is constructed with an opaque metal coating with transparent windows which allow ultraviolet (UV) light to expose specific features.

In this project, the substrate we used to grow ZnO films was sapphire, an insulator, which means that we could not deposit Ohmic contacts on the backside of the sample. To solve this problem, we designed one set of masks to pattern the sample surface and deposit both rectifying and Ohmic contacts on the ZnO surface. The rectifying regions consisted of circles of different sizes, while the area in between was covered with Ohmic contact metal as a uniform electrode. (Fig3.1)

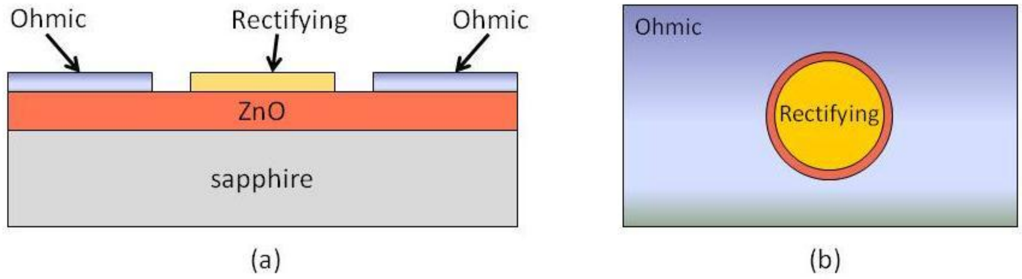

Figure 3.1 Schematic of devices for (a) side view (b) top view.

Two masks were designed to fabricate rectifying contact devices. The first mask was used to pattern the outer circle for the Ohmic contact deposition (Al). The second mask was then used to pattern the inner circles for rectifying contact deposition. Fig 3.2(a) shows the schematic of mask 2. The purple area is patterned for the rectifying contact (Au). The schematic of mask 1 is similar to mask 2 but the diameter of the circles on mask 2 is larger. A 10-µm gap between the inner and outer circles ensured electrical isolation between the Ohmic and rectifying contact metals. The diameters of the inner and outer circles are listed below:

inner diameter (µm)	500	250	100	50
outer diameter (µm)	520	270	120	70

Table 3.1 Diameter of rectifying contact circles as designed.

Another set of masks was designed to fabricate devices for TLM measurements. The first mask was designed to pattern the area for mesa etching. The second mask was used to

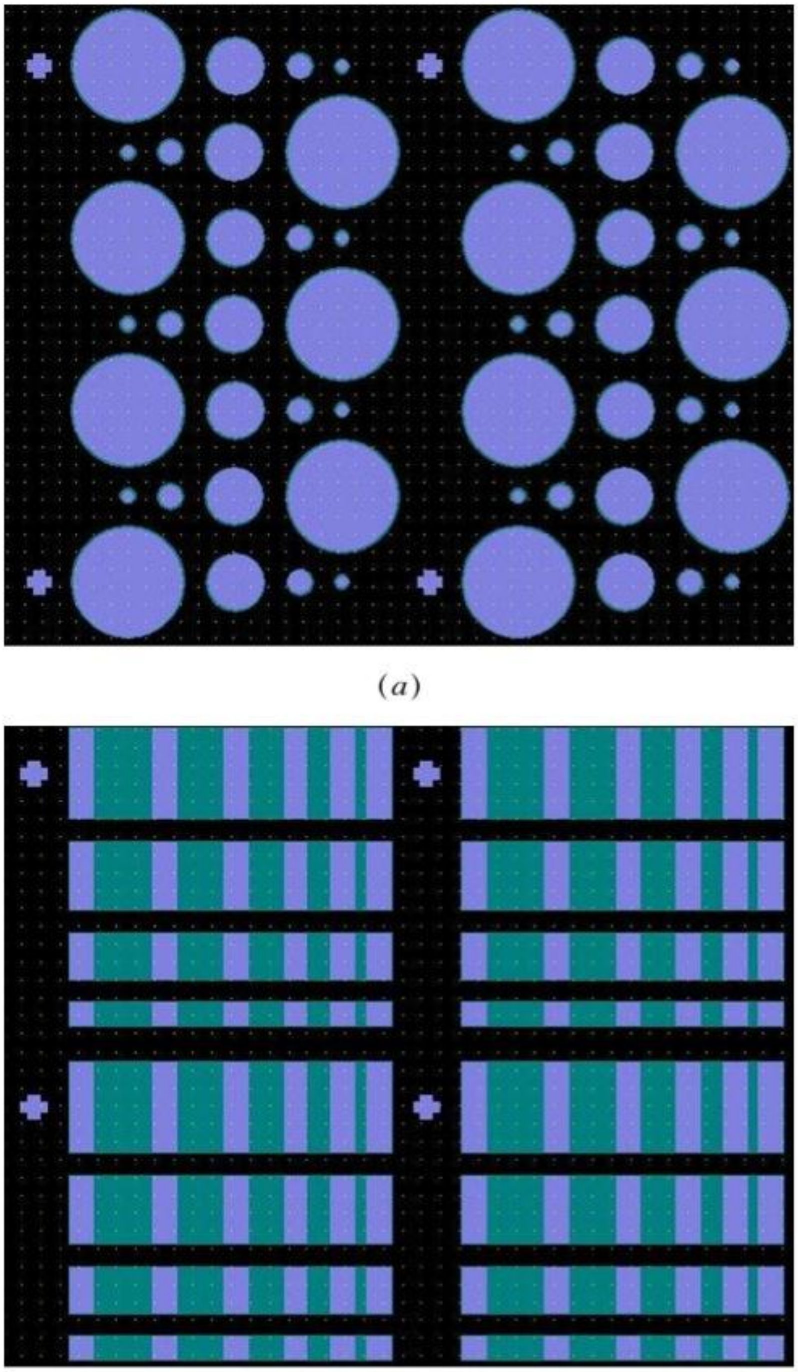
(a)

(b)

Figure 3.2 (a) Mask for fabricating rectifying Au contacts. Light areas represent regions where light passes through. Al mask is similar but with larger circles and the light and dark areas are reversed. (b) superposition of two masks used to fabricate TLM samples. Green shows exposed ZnO surface of mesa. Purple shows Al contact area.

pattern the area for Al (Ohmic contact) deposition on top of the mesas. Alignment marks were added to make sure the two layers did not overlap and that the Al was deposited on the mesa. In fig 3.2(b), the green area is the ZnO mesa and the purple area are Al pads. The masks were fabricated by 4D LABS staff and the patterned area had dimensions of 2 inch×2 inch. The minimum feature dimension was 5 µm and misalignment was within ±1 µm.

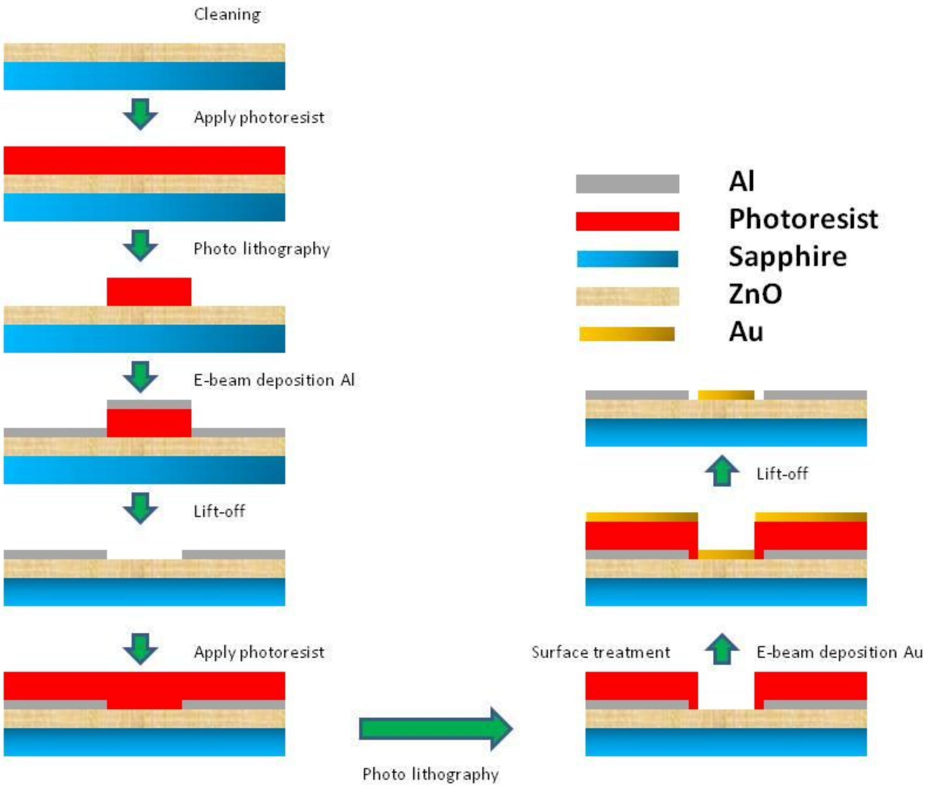

Figure 3.3 Fabrication procedure for rectifying contact devices.

1. Cleaning:

The samples were cleaved into small pieces, ultrasonically rinsed in acetone, iso-propanol and DI water separately, each step for 5 minutes and then dried in flowing nitrogen gas.

2. Photoresist application

Before applying photoresist to the surface of the sample, we added a pre-baking step at 100˚C for one minute, to remove residual water from the surface of the sample, which cannot be removed just by flowing nitrogen gas. This pre-baking can remove water droplets on the sample surface to make the photoresist coat the ZnO film better. Generally, there are two kinds of photoresist: positive and negative. Positive photoresist is removed after exposing to UV light while negative photoresist remains after exposure under UV light. We used AZ 703, a positive photoresist for fabrication, since positive photoresist always yields better process control in small-geometry structures. [12] Samples were mounted on a vacuum chuck in a spin coater. The thickness of the photoresist was determined by two factors: viscosity and spinning speed. The thickness of the sample is inversely proportional to square root of the spinning speed. From experience, 4000 rpm for 1 min is enough for the ZnO samples. The photoresist is very uniform with a thickness of about 1.4 µm under these conditions. After applying the photoresist, a soft bake at 90˚C for one minute was used to solidify the photoresist to prevent damage during the subsequent exposure step.

3. Exposure and development

The photoresist was then exposed through the mask with high-intensity 220 nm UV for 3-4 seconds. AZ 703 photoresist was washed away by developer after exposure to UV light, leaving bare ZnO in the exposed area. The sample was then baked at 110˚C for 1 min, also known as the hard bake, and then placed into AZ 703 developer for 50 sec. The sample cannot be developed too long, since this will start to remove the unexposed photoresist. If the exposure time is too short, photoresist residue will be left in the exposed areas. The sample was then rinsed with DI water and dried with flowing nitrogen gas.

4. Al deposition and lift-off

After opening windows on the photoresist layer, a thermal evaporation system was used to deposit 100 nm of Al on the sample in order to define the Ohmic contact. The sample was then ultrasonically rinsed in acetone in order to lift-off the Al layer attached to the remaining photoresist. Up to this point, we have successfully patterned the outer circles using the first mask and deposited an Al layer as the Ohmic contact.

5. Au contact inner circle definition

Next we repeated steps 2 and 3, with the second mask to pattern the inner circles. During exposure, alignment markers on the masks were used to align the second level of lithography, making sure the outer circles and inner circles did not overlap. Inevitably, there were some lateral errors and rotational errors between the two patterned areas. However, considering there is a 10 µm gap between the inner and outer circles, these errors were tolerable.

6. Surface treatment and Au deposition

Before Au deposition, the sample was usually treated with oxygen plasma or hydrogen peroxide to make a better rectifying contact. The surface treatment condition will be discussed in later chapters. A thermal evaporator was used to deposit Au, followed by lift-off of the excess Au. Finally the sample was cleaned with DI water and dried with nitrogen gas. After this step, the device was ready for current-voltage measurements. Figure 3.4 shows a typical optical microscope image of the final device.

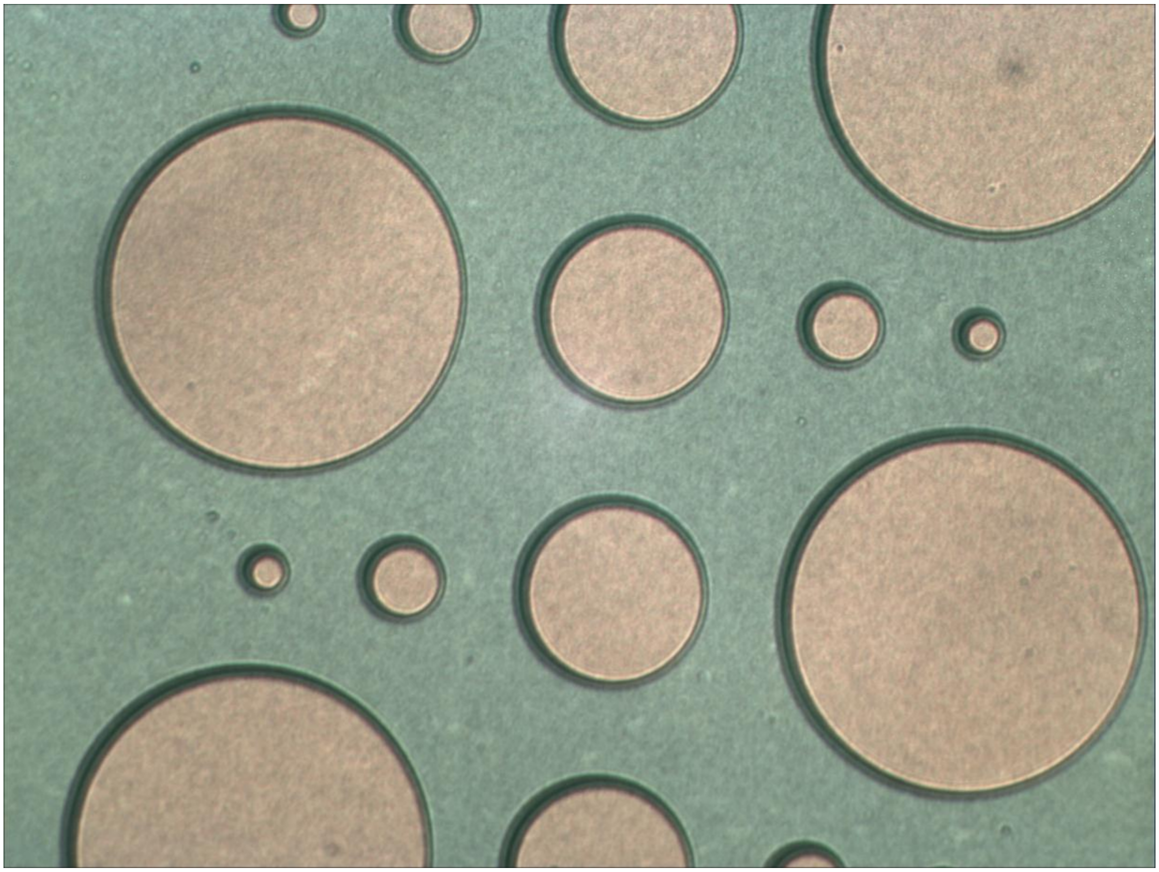

Figure 3.4 Optical microscope image of a typical device after processing (H085). Diameter of the largest Au contacts is 500 µm.

A similar fabrication procedure was also necessary for making devices for TLM measurements. The theory of TLM measurements were introduced in Chapter 2. Fig 3.5 briefly introduces the procedures for device fabrication of TLM samples. The ZnO sample was first cleaned in acetone, iso-propanol and DI water, each step for 5 min, and photoresist was then used to pattern the sample. The sample was then etched in dilute H_3PO_4 (10%) for 1.5 min to form ZnO mesas. The etch rate for 10% H_3PO_4 was about

300 nm per minute. [13] The etching time cannot be too short because that will leave residual ZnO material on the non-mesa area. This will cause current lines to spread during the TLM measurement. On the other hand, if the etching time is too long, a lateral etching effect will occur.

After removing the photoresist, a mesa was formed on a ZnO layer. Then the second mask was used to pattern the Al deposition area on the sample and then Al was thermally evaporated on the mesas. After lift-off and a blow-dry in nitrogen gas, the device was ready for TLM measurements. Fig 3.6 shows a typical optical micrograph of a TLM sample:

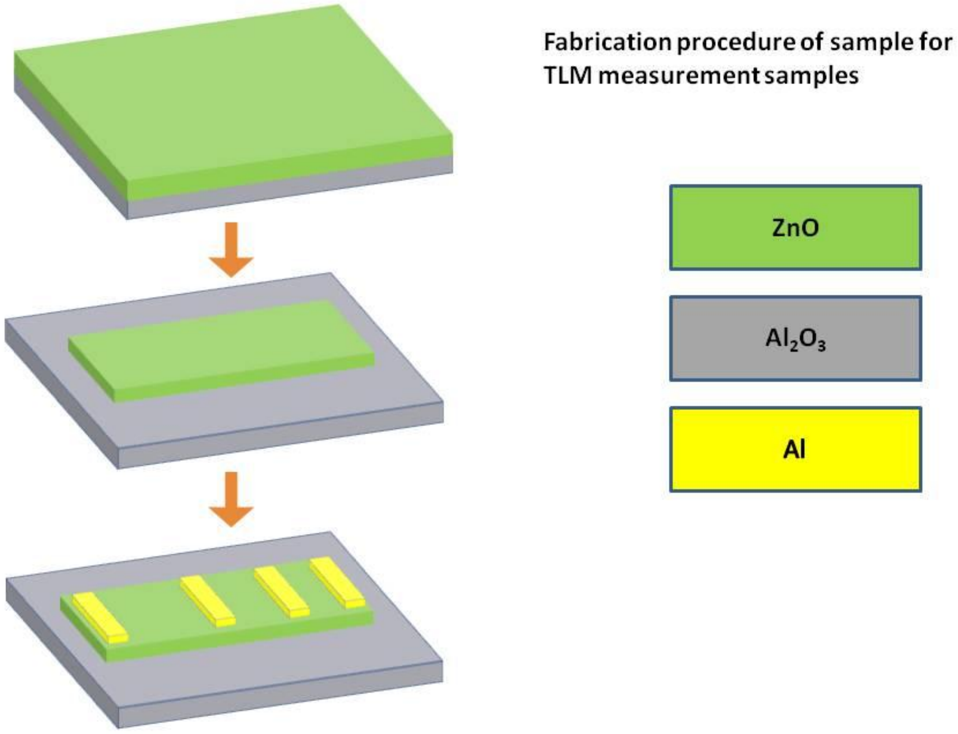

Figure 3.5 Fabrication procedure for TLM samples.

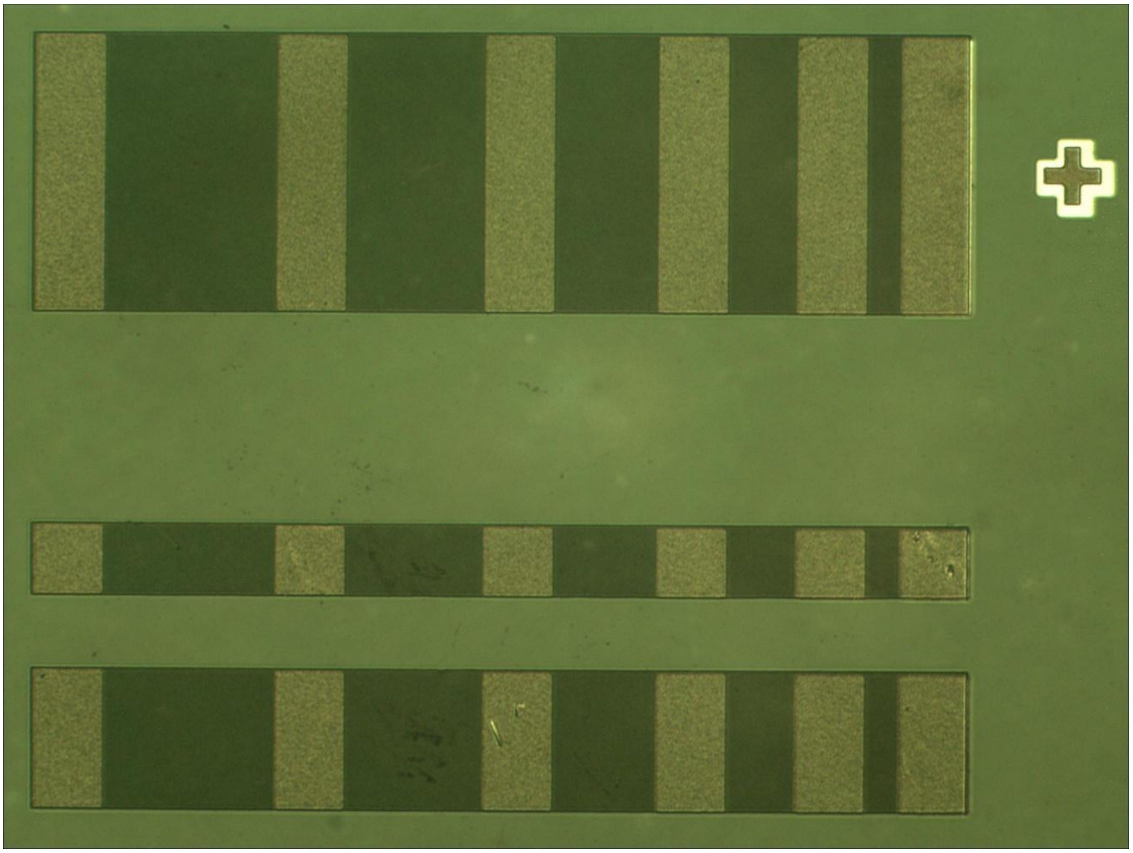

Figure 3.6 Optical micrograph of a typical device for TLM measurement (H075).

3.2 Procedure for preparation of Hall measurement samples

There are several steps to prepare a sample for Hall measurements .

1. The ZnO was first cleaned in acetone and isopropanol to remove the surface contamination and then dried in nitrogen for Hall measurement.
2. In balls were pressed and cleaved into small pieces, and then placed in isopropanol for 5 minutes to remove hydrocarbons.
3. The In pieces were then dried with nitrogen gas and placed into 5% HCl with ultrasonic agitation to remove the oxide on the surface of In.

4. The In pieces were then cleaned in isopropanol and DI water to remove the residual HCl on the surface of the In, followed by a blow dry in nitrogen gas.
5. The In contacts were then pressed firmly onto corners of a ~1 cm square ZnO sample using the wide end of a pair of plastic tweezers.

4: MATERIAL PROPERTIES

The materials properties of ZnO grown by MOCVD are very important, since they may affect the quality of Au-rectifying contacts, which is the primary subject of Ch. 5. In this chapter, a comparative study of ZnO films grown on sapphire (001) and Si (111) substrates by MOVPE will be presented followed by a study of the effect of In doping, annealing temperature and substrate cleaning on the electrical properties of ZnO epilayers.

4.1 Comparison of structural properties of ZnO films on Si and sapphire substrates

ZnO has a hexagonal wurtzite crystal structure. Because of the high cost of single crystal ZnO substrates, most work has focussed on the growth of ZnO on substrates with large lattice mismatch such as sapphire and Si (111). There are significant problems associated with the very large thermal expansion mismatch (56%) and lattice constant mismatch (15.4%) between ZnO and Si resulting in high amounts of tensile strain. [14] This results in very high dislocation densities and the possibility of epilayer cracking, as well as degradation of the optical and electrical properties. [15]

The growth of ZnO on sapphire (001) substrates suffers from similar problems as Si (111) and even after 30° rotation to reduce lattice strain, there still exists an 18.4% in-plane lattice mismatch. [2] In this case the films are under residual compressive strain. [16] The thin film ZnO in this study was grown by MOCVD on Si (111) and sapphire (001) substrates separately at 800˚C. X-ray diffraction for both samples has been performed by the SFU group in a former work. [17] Fig 4.1 shows comparison of the *ω* scans for the ZnO (002) peak for growth on Si (111) and sapphire (001). The full width at half maximum (FWHM) shown in ω scans for ZnO (002) on Si (111) was 7.2º, much larger than the FWHM of 0.1º for ZnO films on sapphire substrate. The peak intensity of ZnO films on sapphire substrate is 4 times higher than for ZnO films on Si substrates. Compared with ZnO grown on Si (111) substrates, ZnO films grown on sapphire (001) substrates have much better crystal quality and are aligned much better along the *c*-axis. However, *ω* scans can only indicate good alignment of ZnO crystal along the *c*-axis; they cannot provide insight into the in-plane alignment.

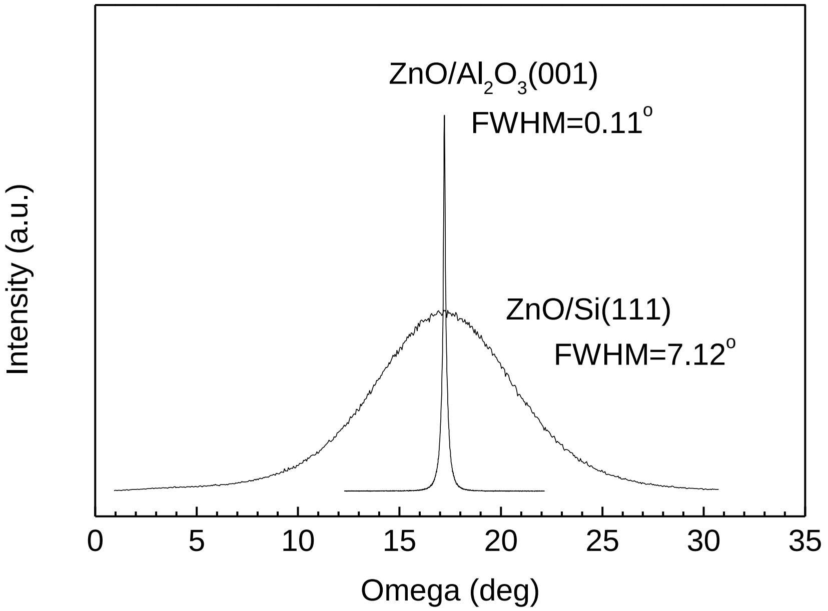

Figure 4.1 XRD ω scan for the ZnO(002) plane grown on Al_2O_3(001) and Si(111) substrates performed by David Huang.

To investigate the in-plane alignment of ZnO films, (101) XRD pole figure scans were performed. Because of the wurtzite structure of ZnO, a 6-fold symmetry of the (101) peak should be observed around the c-axis if the crystals are well aligned in-plane. The detector was fixed at $2\theta = 36.4°$ corresponding to the (101) reflection, while the azimuthal angle $\emptyset$ and tilt angle ψ were varied. Fig 3.2 shows the pole figure result for ZnO growth on sapphire substrates by MOCVD at 800˚C. ψ was varied from 56.0 to 68.0° and $\emptyset$ was varied from 0-360°. It can be seen that there exist 6 peaks separated by 60° along the φ axis. This result indicates that ZnO layers on sapphire substrates are not only aligned along the c axis but also showed good in-plane alignment. [18]

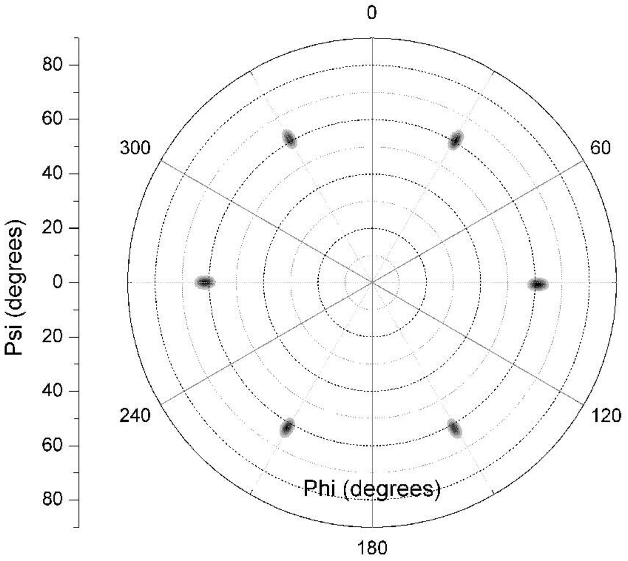

Figure 4.2 (101) Pole figure for ZnO on a sapphire substrate.

If the tilt angle is fixed at the average optimized tilt angle for these six peaks, the two dimensional pole figures reduces to a $\emptyset$ scan. Fig. 4.3(a) shows a $\emptyset$ scan from the previous ZnO sample grown on sapphire, derived from the pole figure data with a fixed tilt angle of 60.8°. Fig. 4.3(b) shows the ∅ scan taken for the sample but with the tilt angle and 2θ set to the (202) diffraction condition of the sapphire substrate. The scan shows three very narrow peaks with much higher peak intensity than the ZnO peaks. Each peak is separated by 120° showing the 3-fold symmetry of Al_2O_3 around its *c* axis. There exists a 30° shift between the sapphire (202) peak and the ZnO (101) peak confirming that there is a 30° rotation between the ZnO and Al_2O_3 (101) directions. This 30° rotation occurs because the ZnO lattice aligns itself with the oxygen lattice in Al_2O_3 during the growth in order to decrease the in-plane lattice mismatch between Al_2O_3 and ZnO from 34% to 18%. [19]

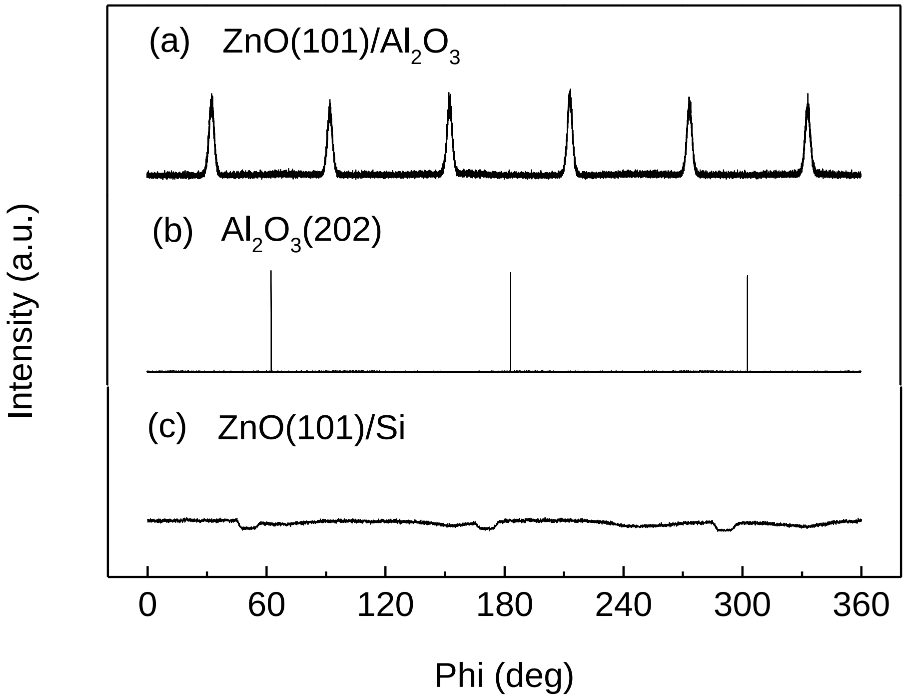

Figure 4.3 XRD φ-scan for (a) ZnO/Al_2O_3 (101) plane scan, (b) Al_2O_3 substrate (202) plane scan, (c) ZnO/Si (101) plane scan performed by David Huang.

Fig. 4.3 (c) shows the ∅ scan for ZnO growth on a Si (111) substrate. It shows a flat pattern with roughly uniform intensity and no significant peaks. This shows that the ZnO crystal growth on Si (111) was randomly oriented around the *c*-axis. This conclusion agrees with TEM data and selective area electron diffraction (SAED) images of a ZnO film grown on a Si (111) substrate shown in Fig 4.4 (performed by Weiyang Jiang, analyzed by the author D.C. Li.). The rings in the SAED image confirm that the ZnO grains are randomly oriented in the growth plane in agreement with the φ-scan result. Otherwise, there should be another set of spots, not rings, corresponding to the ZnO lattice. The indices indicated in Fig. 4.4 were verified by calculating the distance from the center of the main beam, calibrated via the Si substrate spots..

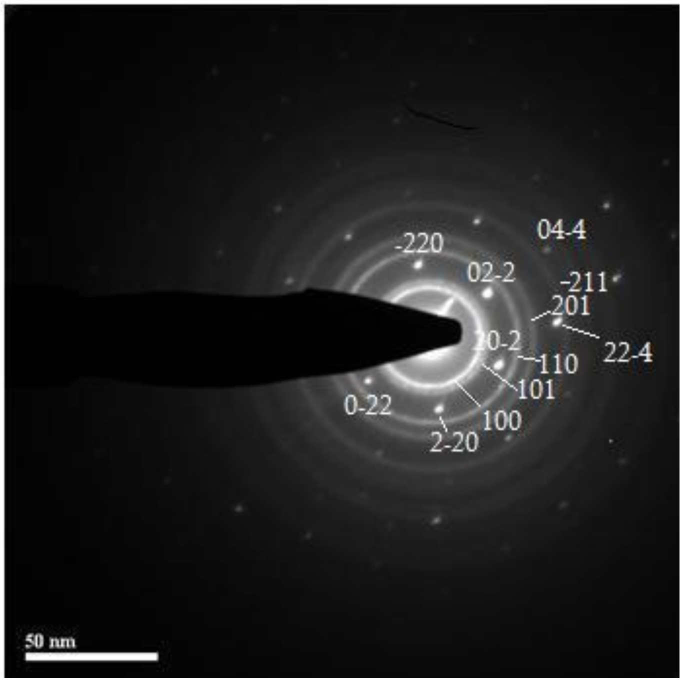

Figure 4.4 Selective area electron diffraction (SAED) images of ZnO film grown on Si (111) substrate.

This random in-plane ZnO lattice orientation may be due to the presence of a thin amorphous SiO_2 layer formed on the Si surface before ZnO deposition since Si is easily oxidized in N_2O. [20] Some reports suggested the growth of a ZnO buffer layer between the ZnO film and the Si substrate may solve this problem. [21-22]

4.2 Electrical properties

The fabrication of electronic devices from ZnO is an active and ongoing area of research. Controlled doping has proven to be very challenging. *n*-type doping is relatively easy compared with p-type doping [2] since most as-grown ZnO is naturally n type due to the existence of native defects such as Zn interstitials (Zn_i) and oxygen vacancies (V_o), although the exact role of these two native defects is still controversial. Look has suggested that Zn_i rather than V_O contributes to the conduction, but in the form of a defect complex, with an ionization energy of about 30-40 meV. [23] It was also suggested by Van de Walle that hydrogen can be the dominant background donor since hydrogen is present in most growth methods, [24] however hydrogen appears to desorb from films grown at high temperatures and was not observed in photoluminescence measurements of our MOVPE films.[16] Group III elements such as Al, Ga, and In have been investigated as *n*-type dopants since they can substitute for Zn atoms and bond with O to provide one extra donor electron.[23] Group III element dopants have been attempted by many groups and ZnO films with high conductivity have been reported. [25-26]

In this work, the effect of controlled In and Al doping on the electrical properties were investigated using Hall effect measurements. Besides doping effects, the effect of substrate cleaning and post-growth annealing was also investigated. For the samples grown in this study, dimethylzinc (DMZn) and N_2O were used as the Zn and O precursors, and trimethylindium (TMI) and trimethylamine alane (TMMA) were used as the In and Al sources. The effect of substrate treatments on doping was investigated. ZnO epitaxial layers were grown on annealed or untreated substrates by MOVPE at 800˚C. When pre-growth annealing was used, it occurred at 1100˚C in a tube furnace for 30 min with pure oxygen at a flow rate of 100 sccm. Sapphire substrates were obtained from Silian Corporation, Victoria BC and were C-plane ±0.2°.

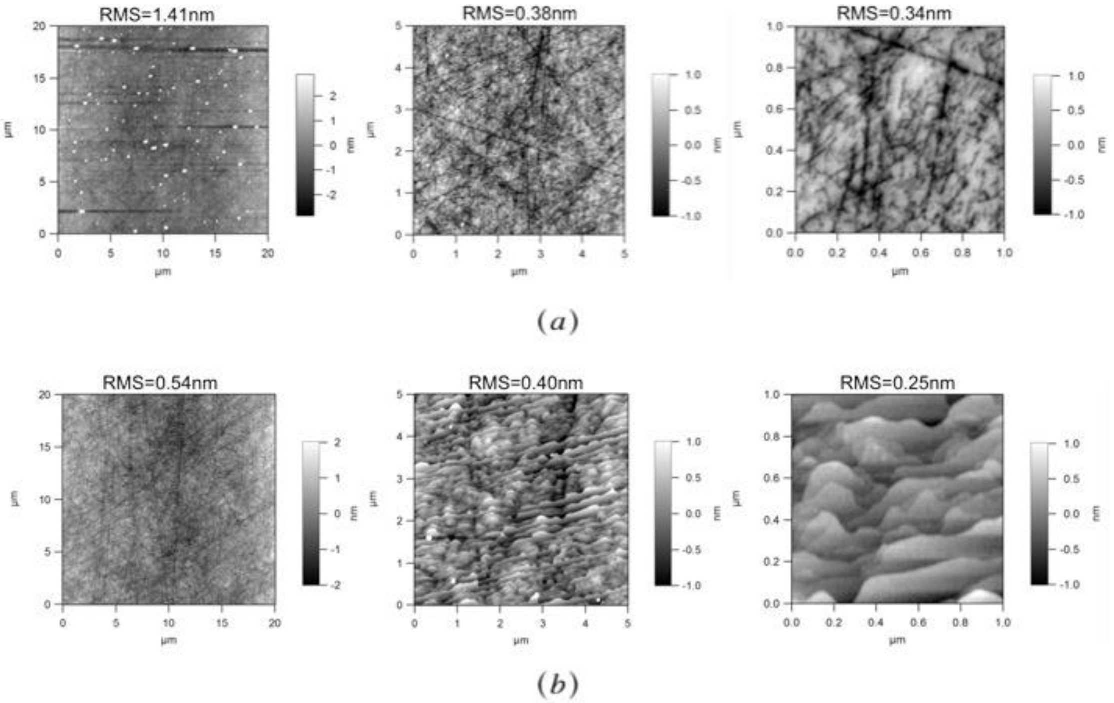

Figure 4.5 AFM images of sapphire (Al_2O_3) substrate for (a) no annealing and (b) annealing at 1100˚C for 30 min with 100 sccm oxygen flow. [27]

Fig 4.5 shows a comparison of the surface morphology of the sapphire substrate before annealing and after annealing in 1100 ˚C oxygen for 30 min. Before annealing, there are random scratches and small particles on the substrate. The scratches may come from the polishing procedure and the small particles were likely due to polishing compounds.

After annealing, the substrates show a low particle density and atomic terrace steps indicating that the surface damage layer has been removed. The formation of atomic terraces might be helpful for ZnO film growth by improving nucleation on the surface. The absence of particles after annealing suggests that the particles may be carbon related clusters which are burned off after high temperature annealing. [27] Surface roughness was considerably improved by annealing the sapphire substrates in a tube furnace at 1100°C for 30 min.

To investigate the effect of In doping, a series of samples was grown with TMI flows ranging from 0 to 20 sccm. Two series of samples were grown at 800 ˚C, on pre-treated sapphire and as-received sapphire. The treatment consisted of cleaning in organic solvents followed by annealing in oxygen at 1100°C. Figs. 4.6 (a) and (b) shows a comparison of the effect of In doping on the electron concentration and mobility respectively for samples grown on annealed sapphire substrates versus as received substrates. The hollow point shows data from a second Hall sample from the same growth. For undoped samples (TMIn=0), the carrier concentration for the annealed substrates shows a significant decrease and the mobility nearly doubled compared with growth on un-treated substrates. This is probably related to the strong difference in surface morphology indicated by the previous AFM results. Surface pre-treatment by substrate cleaning and O_2 annealing results in the formation of atomic terraces indicating clean oxygen terminated sapphire surfaces. (Fig. 4.5) The nucleation of ZnO will tend to occur uniformly on such a surface, resulting in a layer-by-layer growth mode. In contrast, residual surface contamination of the untreated substrate will inhibit two-dimensional growth. Instead, nucleation will occur less uniformly at specific sites resulting in the lateral coalescence of grains. The lower mobility of the ZnO samples grown on untreated substrates may be due to the presence of charge scattering at crystal grain boundaries. [28] Also, scanning electron microscopy measurements showed that the morphology of the samples grown on untreated substrates consisted of closely packed rods, compared to a more continuous films with some voids for samples grown on treated substrates. [29] The increase of the carrier concentration for the untreated sample may due to the increase of native defects and larger effective surface area caused by the 3 dimensional growth.

The effect of In-doping is somewhat different for the treated vs. untreated substrates. Surprisingly, there is a weak decrease in carrier concentration with increasing In doping for samples grown on as-received substrates. This may be due to the higher background doping masking the weak effect of In doping. One possibility is that In forms complexes with the native donors, reducing the free electron concentration. This assumption obviously needs further work to verify.

In contrast, there is a small increase in carrier concentration with In doping for samples grown on heat treated substrates. This effect may occur because of the lower background doping on treated substrate due to a significant improvement in the surface roughness and film quality.

Low temperature photoluminescence (PL) measurements [16] and secondary ion mass spectrometry (SIMS) confirmed that there is In incorporated in the layers. PL results show the appearance of emission lines due to the excitons bound to neutral and ionized In donors. [16] Table 4.1 shows SIMS data and Hall data for pre-treated substrates.

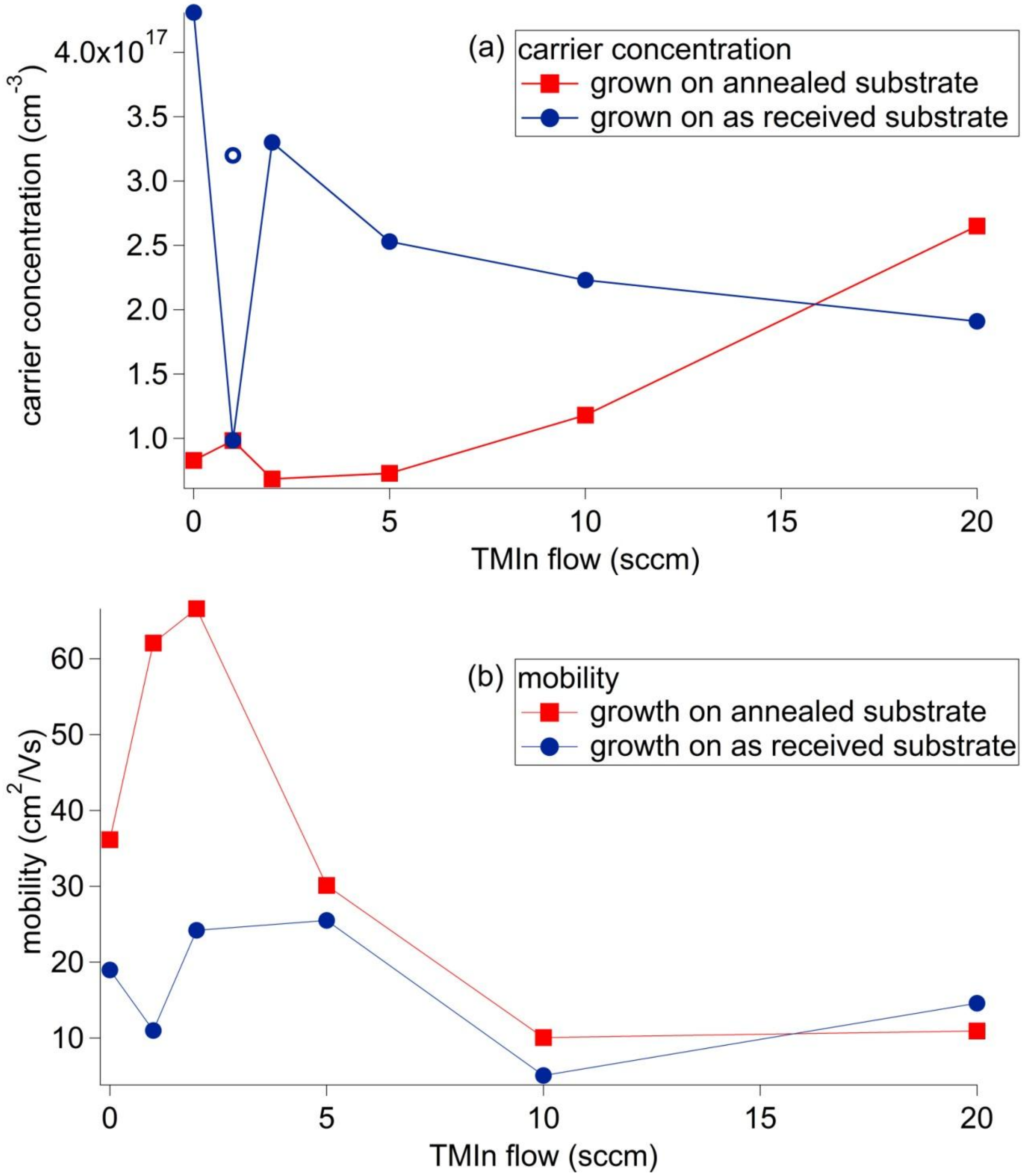

Figure 4.6 300K (a) carrier concentration and (b) mobility as a function of TMI flow for samples grown on treated and untreated substrates.

TMI flow (sccm)	**n (Hall) (cm^{-3})**	**[In] (SIMS) (cm^{-3})**	**XRD FWHM**
0	4.31×10^{17}	2.0×10^{19}	0.182
2.0	2.53×10^{17}	4.1×10^{18}	0.188
5.0	9.84×10^{16}	1.7×10^{19}	0.247
10.0	2.23×10^{17}	9.4×10^{19}	0.338
20.0	1.91×10^{17}	1.7×10^{20}	0.577

Table 4.1 Electron concentrations from Hall measurements, and SIMS In concentrations for different In flows.

SIMS analysis was performed on a 1.1 µm ZnO thin film with different In doping concentrations in order to obtain a depth profile of total In concentration. [30] (Fig. 4.7) The structure of the SIMS sample consisted of 5 layers of In doped ZnO with TMIn flows of 0 (undoped), 2.0, 5.0, 10.0, and 20.0 sccm. The SIMS data show a huge discrepancy between the actual In concentration and the measured electron density, indicating that the majority of the In does not form shallow substitutional donors. A similar, although smaller effect, was reported previously in a recent paper on In doping of ZnO grown on GaN epilayers. [31] This may be due to the formation of other indium oxide phases such as In_2O_3, although these were not observed in XRD measurements.

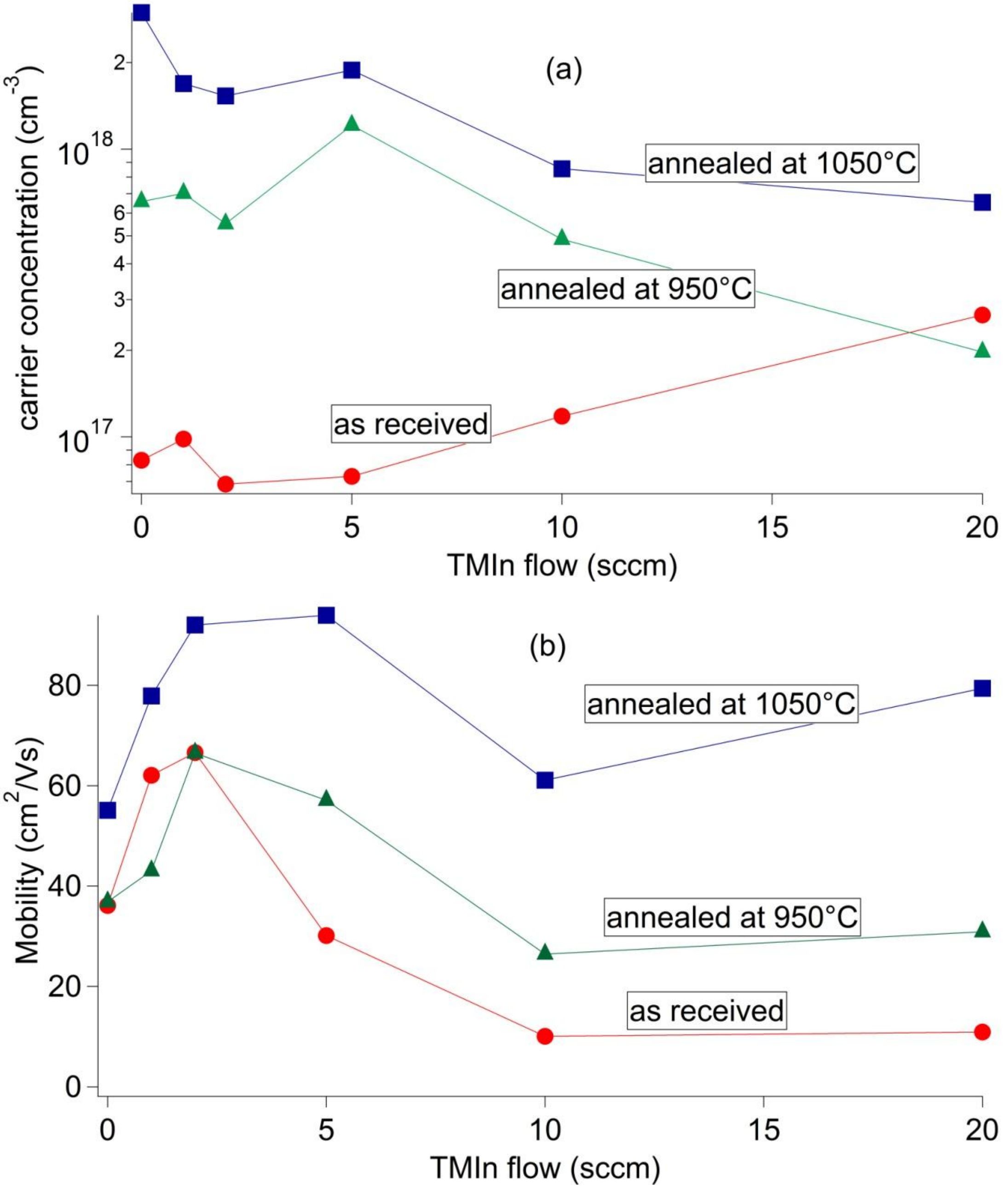

Figure 4.7 Hall measurement for (a) carrier concentration (b) mobility as a function of TMI flow and annealing temperature. Substrate was treated in O_2 at 1100°C prior to growth.

In an unsuccessful attempt to improve the activation of donor, we performed post-growth annealing of a series of In-doped epilayers. Fig 4.7 shows the carrier concentration and mobility as a function TMI flow for different post-growth annealing conditions. Also shown are the previous samples without post-growth annealing. All of these samples were grown on pre-treated substrates (cleaned in solvents plus an O_2 anneal in the tube furnace at 1100°C). The samples were given a post growth anneal at 950°C and 1050°C annealing respectively.

Fig. 4.7(a) showed that annealing greatly increased the carrier concentration, for both doped and undoped samples. This has also been observed by other groups who attributed it to the formation of native donor defects. [32] For the samples with no post-growth annealing, the carrier concentration increased somewhat with In-doping as discussed previously, while for the post-growth annealed samples, the carrier concentration showed a large increase for the undoped layers, but a steady decrease with increasing In doping level. It is clear that high temperature annealing is increasing the background doping possibly through the formation of native defects, and that these are masking the effect of the In doping on the electrical properties.

Fig 4.7 (b) shows the 292K mobility as a function of TMIn flow and annealing temperature. Annealing increased the mobility for nearly all doping levels. Normally an increase in donor concentration results in a decrease in mobility due to increased ionized impurity scattering, however we see the opposite behaviour. We should point out that the expected theoretical mobility for ZnO at a doping level of $10^{17}cm^{-3}$ is around 200 cm^2/Vs at room temperature. [33] The observed improvement in mobility by annealing may be due to improvements in the crystal microstructure by annealing: Annealing has been shown to improve the structural properties of ZnO. [16] Fewer grain boundaries should increase the effective mobility by reducing charge carrier scattering at grain boundaries. The mobility has the same trends for both annealing temperatures. The mobility increases noticeably for small In concentrations which may be due to the reduction in free carrier concentration caused by partial compensation of native defects by In atoms or complexes. The mobility reaches a maximum value at around 2-5 sccm TMIn flow and then decreases at higher values. This suggests that high concentrations of In result in the formation of additional scattering centres. XRD measurements showed an increase in the ω-scan FWHM from 0.18 to 0.58 as the TMIn flow increased from 0 to 20 sccm. (Table 4.1) This indicates the formation of additional structural defects at high concentrations which could also produce additional charge scattering. This is also confirmed by the PL results which show a strong decrease in PL intensity with high In doping. [16]

Similar trends were observed in a series of Al doped samples shown in Fig 4.8. These samples were grown using trimethylamine alane (TMMA), which is a low vapour pressure precursor with no Al-C bonds. These samples were grown on pre-treated sapphire, annealed at 1100 ˚C. PL measurements on these samples confirmed the presence of shallow Al donors. The Hall data indicate a possible increase in electron concentration with doping, however the data are scattered and further work is clearly needed. Further improvements in crystal structure and morphology will be required to properly investigate the effect of group III dopants. For example, by growing on ZnO substrates, it is possible to greatly improve the morphology and structural quality. *C-V* measurements as discussed in Chapter 5 could then be used to measure the donor concentration in samples with low native and structural defect concentrations.

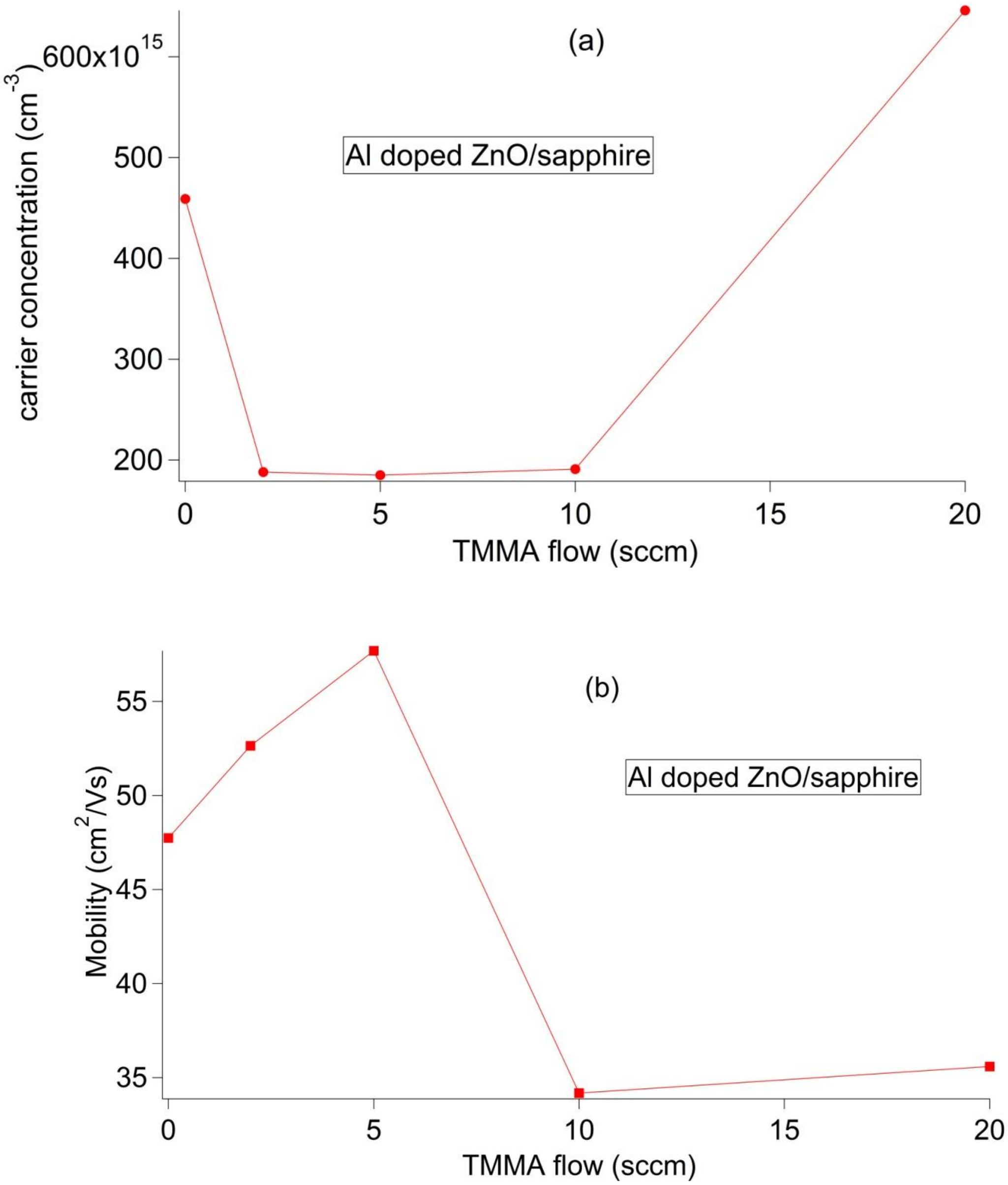

Figure 4.8 Hall measurement for (a) carrier concentration (b) mobility as a function of TMMA flow and annealing temperature. Substrate was treated in O_2 at 1100°C prior to growth.

Hall measurements were also carried out as a function of temperature in order to extract the donor binding energies and donor concentration in selected undoped and In-doped ZnO films. The theory of this part has been discussed in former chapters. The relationship between electron concentration and temperature can be well fitted using the charge-balance equation (CBE) in a single-donor model: [23]

$$n + N_A = \frac{N_D}{1 + n/\phi} \tag{4.1}$$

where n is the electron concentration, N_A and N_D are the acceptor and donor concentrations to be fitted. ϕ is given by:

$$\phi = (1/g)N_C T^{\frac{3}{2}} exp(-E_D/kT) \tag{4.2}$$

Here, g is a degeneracy factor. $N_C = 2(2\pi m_n^* k)^{3/2}/h^3$ is the effective conduction-band density of states at 1K. E_D is the donor activation energy. N_D, N_A and E_D are treated as fitting parameters in order to model the measured electron concentration obtained from Hall measurements.

Fig 4.9 (a) and (b) show a comparison of temperature dependent Hall data for an undoped sample and a sample with a TMIn flow of 1.0 sccm. The samples were prepared without post-growth annealing. The carrier concentration vs. inverse temperature was plotted in Fig 4.9 (a) and fitted to equation 3.1. We fixed the shallow acceptor concentrations at 10^{15} cm^{-3}. We assumed $N_A \ll N_D$ since our PL data indicates that there are almost no detectable shallow acceptors in our material. [16] The parameters extracted from the fits are summarized in Table 4.2. Both samples show freeze-out of the electron concentration between 300K and 240K due to capture of free electrons by shallow donor ions at low temperatures. The donor activation energy extracted in this range was between 30-40 meV (Table 4.2), much lower than the expected value for In (63.2 meV) suggesting that In is not the dominant donor responsible for the electron concentration. [34] The undoped sample also has a similar binding energy as the In-doped sample. PL indicates that Ga is the dominant shallow donor in our undoped material. [16] However, the binding energy of Ga is 54.6 meV, which is still much larger than the observed donor activation energy. Also, the SIMS measurements showed a Ga concentration of around 3×10^{16} cm^{-3}. These data suggest that native defects, rather than In or Ga donors, dominate the conduction of these two samples.

Below 240K, the electron concentration did not continue to decrease with decreasing temperature as predicted by equation 3.1, which indicates the presence of an additional conduction channel, which dominates the conductivity at lower temperature. Similar results have been observed for both thin film and bulk ZnO samples. [35-38] It was suggested by D.C.Look that there is a highly conductive thin layer due to the highly reactive ZnO surface absorbing impurities such as H or impurities or defects moving from the bulk to the surface during the annealing treatment. [35] At higher temperatures, the bulk part of the ZnO dominates the electron transport resulting in freeze-out as the temperature decreases. At low temperatures, once the bulk carriers are frozen out, the conduction becomes dominated by the high sheet density of the surface conduction layer. This is expected to be especially severe in our films, which have a higher fraction of surface area to volume compared with a perfect planar film.

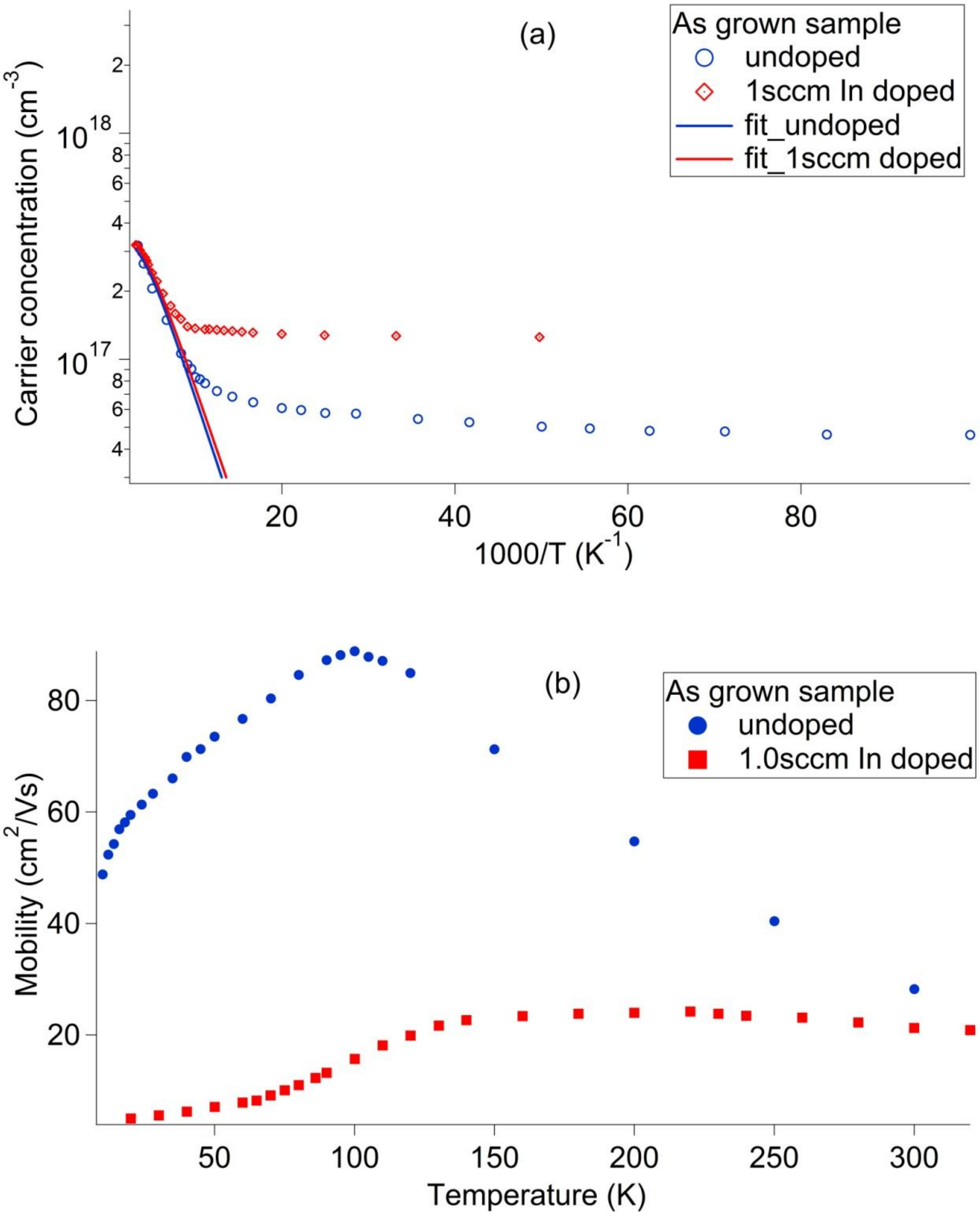

Figure 4.9 (a) carrier concentration (b) mobility versus temperature for an as-grown ZnO with and without 1 sccm of In doping. The sapphire substrate had no cleaning or annealing pre growth treatment. Sample H233 (undoped) and H266 (1sccm TMIn).

Fig 4.9 (b) shows the comparison of mobility for the undoped sample and the 1.0 sccm In doped sample. There are two mechanisms dominating the carrier mobility of bulk semiconductors: phonon scattering and ionized impurity scattering. [39] For the undoped samples, phonon scattering is responsible for the decrease in mobility above 100K and ionized impurity scattering is responsible for the reduction in mobility below 100K. The effect of In doping on the mobility is small at room temperature but very large at low temperatures. This again points out the possibility that In is enhancing the defect concentration in the crystals which is increasing the electron scattering at grain boundaries or point defects.

Sample	TMI flow (sccm)	Donor concentration $(10^{18} cm^{-3})$	Donor energy (meV)	Substrate treatment
Epilayer annealed at 1050°C	0	5.6 ± 0.3	5.3 ± 1	Annealed 1100°C
	5	3.0 ± 0.2	1.8 ± 1	Annealed 1100°C
As-grown epilayer	0	0.36 ± 0.02	37.4 ± 2	No Treatment
	1	0.37 ± 0.01	31.7 ± 1	No Treatment

Table 4.2 Summary of temperature dependent Hall measurements.

The behaviour of the annealed samples is quite different. Fig 4.10 shows a comparison of the temperature dependent Hall data with and without 5 sccm of In doping. These samples were grown on cleaned sapphire substrates annealed at 1100 °C and post-annealed at 1050°C for 30 min. It can be seen from Table 4.2 that the activation energy for freezeout is much lower for these samples. This is due to the greatly increased donor concentration caused by annealing. As previously discussed, annealing increases the concentration of native donor defects, and the activation energy is thereby reduced at high doping due to overlap of the excited donor states.

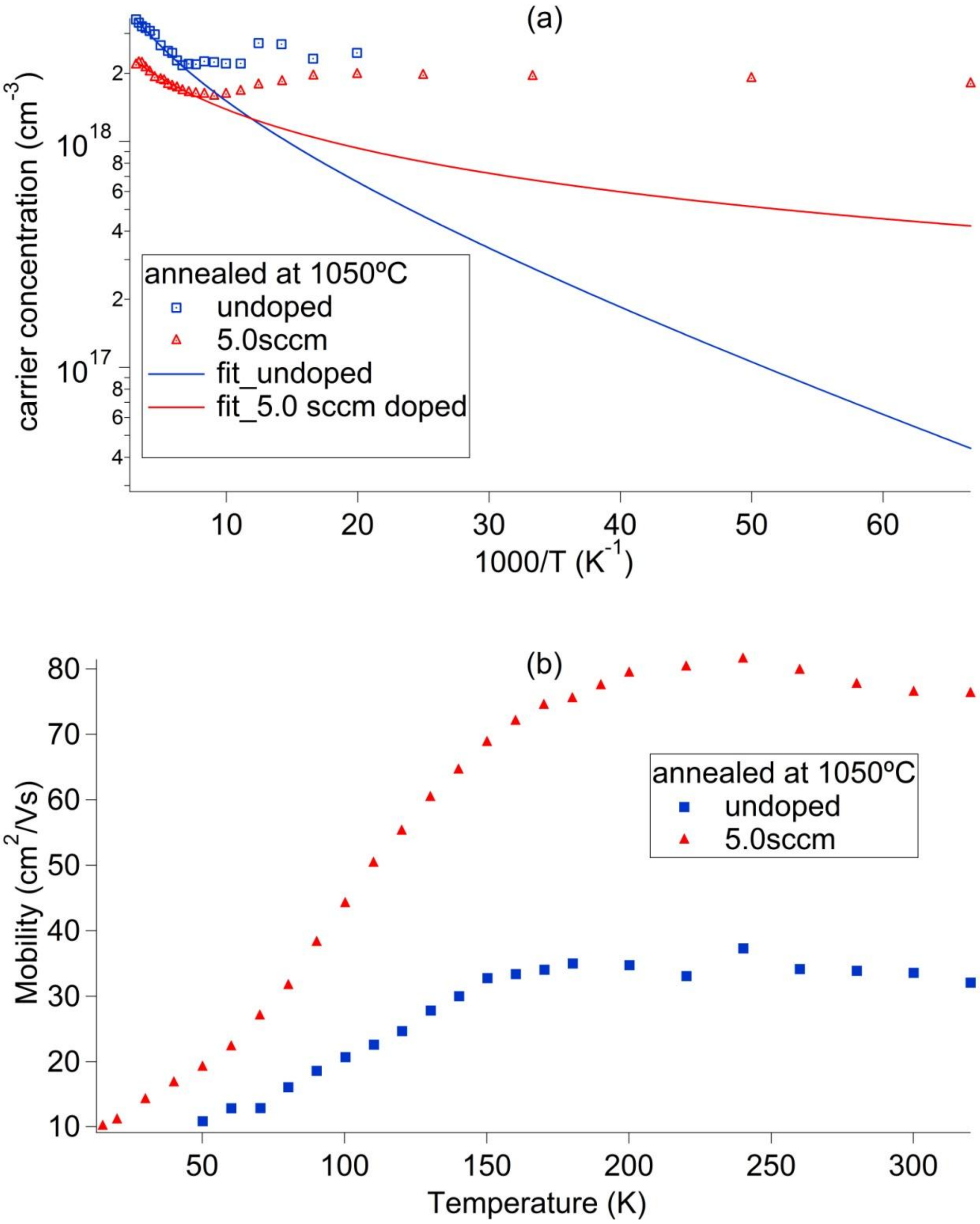

Figure 4.10 (a) carrier concentration and (b) mobility as function of temperature for ZnO samples annealed at 1050°C. Sapphire substrate was cleaned and annealed at 1100°C. Samples H282 (undoped) and H285 5sccm TMIn.

Reduction of the activation energy is typically caused by the formation of impurity bands in the donor excited states, which reduces the activation energy for ionization of an individual donor electron. [40] Also the annealed samples show much less of a freeze-out effect than as received samples, for both In-doped and non-doped samples, indicating a higher electron concentration in the surface conduction layer for the annealed samples.

The low temperature mobility of the 5 sccm In doped sample shows a significant increase in mobility compared with the undoped sample. It is interesting that the surface roughness of this sample was greatly improved, with very few voids and an almost fully coalesced microstructure. [29] The role of In in smoothing the films is a very interesting result that deserves future study. The fact that the mobility for the doped sample is much higher tends to support the earlier statement that much of the poor Hall results come from the 3-d microstructure of the films. Other factors may be relevant, for example the fact that the film is doped with In.

5: METAL-ZnO JUNCTIONS

We have discussed the formation of rectifying Au and Ohmic Al contacts in chapter 2. A rectifying contact is a metal-semiconductor contact with asymmetric current-voltage characteristics, which can be fabricated by choosing a particular metal and substrate with a specific combination of work functions. Although Au is reported to be easy to degrade at high temperature, [41] it is still widely used to make rectifying contacts on both bulk and thin film ZnO by many groups. [42-44] Other metals such as Ag, [45-46] Pd, [47] Pt [48] are also good candidates for making rectifying contacts on ZnO. There are also some reports from the literature that surface treatments such as oxygen plasma, [49] hydrogen peroxide solutions [50] and surface etching in concentrated HCl [51] may improve the quality of rectifying contacts. However, up to now, there have been very limited reports of good rectifying contacts on ZnO, especially for thin film ZnO growth by MOCVD.

To obtain a good Ohmic contact, reducing the contact resistance is an important problem. Many metallization schemes for making Ohmic contacts on ZnO have been studied [52-54], such as Ti/Au, Al/Pt, Ti/Al/Pt/Au and Al, all of which have been proved to be good Ohmic contacts with low contact resistance. Among these metallization schemes, Al is easy to deposit and shows good Ohmic behaviour on ZnO. It was found that O atoms will out-diffuse to the Al metal layer while the Al atoms in-diffused to the surface region forming a layer of *n*-type ZnO:Al. This inter-diffusion increases the doping concentration near the surface making the Al-ZnO contact more linear. [55] For our study on metal-ZnO contact, it is necessary to fabricate a good Ohmic contact with a low contact resistance, in order to investigate rectifying contacts on ZnO, which is a more challenging task.

In this chapter, the results of transmission line measurements (TLM) of Al contacts on ZnO will be presented. Detailed *I-V* and *C-V* measurements for rectifying Au contacts on ZnO will be presented. Also, a qualitative model of contact size effects for rectifying Au contacts on ZnO will be provided, as well as a discussion of the effect of surface treatment on the formation of rectifying Au-ZnO contacts. Details of the growth conditions and Hall results for the layers used in this chapter are given in the Appendix.

5.1 Transmission Line Measurements

The process of fabrication of TLM devices was introduced in Chapter 3. The schematic of the device with dimensions is shown in Fig. 5.1. Mesas were etched to ensure that the current was confined to the ZnO mesa. The widths of the mesas are 110 µm, 210 µm, 310 µm, and 410 µm. Al metal was deposited by e-beam deposition on the mesas with different spacings. There was a 5 µm gap between the Al pads and the mesa edge. The *I-V* characteristics were measured between pairs of Al pads with different separations using a probe station in the cleanroom. Two pieces of ZnO material, H062 and H075 were fabricated for TLM measurements. H062 was grown at 800°C for 60 min while H075 was a two step growth sample. A buffer-layer of ZnO was first deposited at 500°C on sapphire for 5 min and then another layer was deposited at 800°C for 40 min. This two step growth was expected to help obtain material with smoother surfaces, as well as better electrical properties.

Figs. 5.2 (a) and (b) show the results of TLM measurements for samples H062 and H075. Here we just give the results for 100 µm width mesas. The measurements were carried out by moving two probes onto adjacent Al pads with different mesa separations. Then all the *I-V* curves were plotted to obtain the total resistance for different spacings. It is worth pointing out that the measured resistances contain not only the resistance between the two probes but also the resistance of the probe station system, which should be tested before measurement.

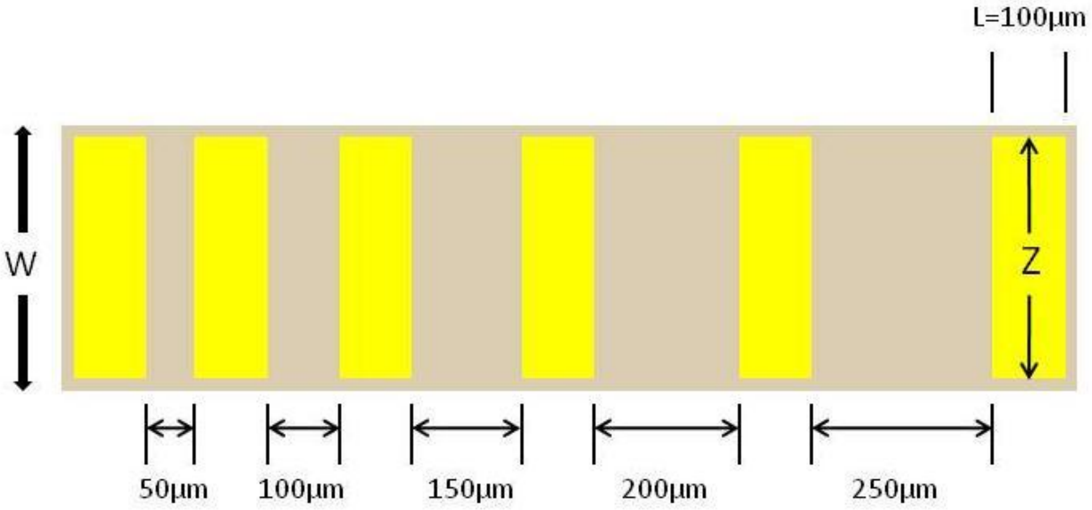

Figure 5.1 Schematic and dimensions of TLM measurement devices: W=110 µm, 210 µm, 310 µm,410 µm; Z=100 µm, 200 µm, 300 µm, 400 µm.

As was discussed in chapter 2, the resistance includes 2 parts: contact resistance and resistance from the ZnO mesa. If we assume the contact resistance is constant, the increase of the resistance with increased spacing between Al contacts was caused by the increased length of the ZnO bar travelled by the electrons. The resistance versus distance plot (Fig 5.2), was a straight line as expected. The resistivity can be extracted from the slope of the line while the y-intercept can give us the contact resistance. The *x*-axis intercept can be used to calculate the specific contact resistivity. The results of TLM measurements for both ZnO H062 and H075 were summarized in Table 5.1 (a) and (b).

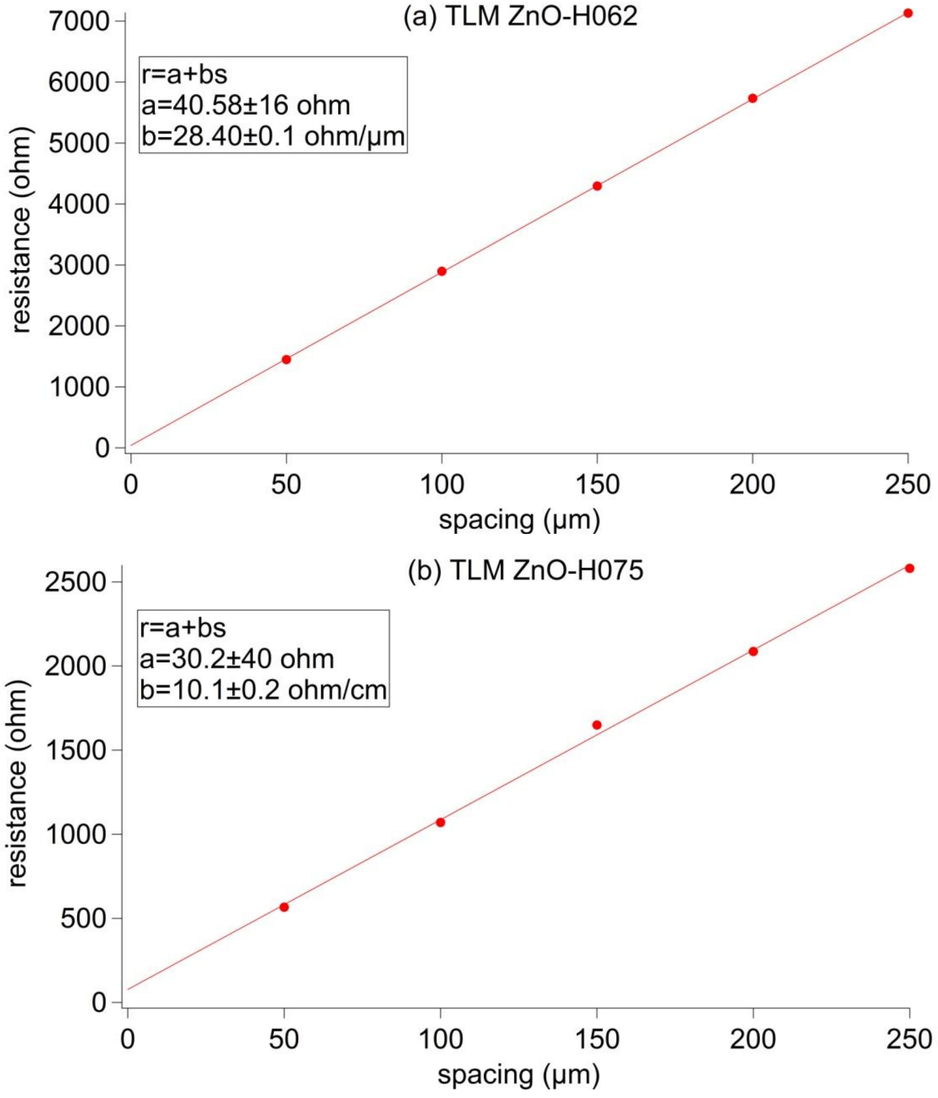

Figure 5.2 TLM measurement on (a) ZnO H062 (b) ZnO H075 with mesa width of 100µm-resistance versus distance.

The resistivity and sheet resistance agreed with each other for all the measurements of different sample widths, as did the value determined from Hall measurements. The resistivity and sheet resistance were obtained from the slope of the straight lines in Fig. 5.2 using equation 2.18. The slope has a very small percentage error so we did not quoted error of the resistivity and sheet resistance.

(a)	Transfer length (μm)	contact resistance (ohm)	Specific contact resistivity (ohm·cm^2)	Resistivity (10^{-2}ohm·cm)	sheet resistance (10^3ohm)
100μm	0.7±0.5	20.0±16	1.49×10^{-5}	6.48	2.84
200μm	2.7±1	38.9±3	2.07×10^{-4}	6.70	2.92
300μm	2.6±1	25.4±4	1.97×10^{-4}	6.64	2.96
400μm	7.9±3	58.7±17	1.85×10^{-3}	6.36	2.99
average				**6.55±0.15**	**2.93±0.07**
Hall measurement result				**6.34**	**2.84**

(b)	transfer length (μm)	contact resistance (ohm)	specific contact resistivity (ohm·cm^2)	Resistivity (10^{-2}ohm·cm)	sheet resistance (10^3ohm)
100μm	1.4±2	15.1±20	3.0×10^{-5}	4.65	1.01
200μm	-3.3±0.4	-17.6±2	1.2×10^{-4}	4.92	1.07
300μm	2.2±3	7.3±8	5.8×10^{-5}	4.55	0.99
400μm	2.7±3	7.1±7	7.7×10^{-5}	4.78	1.04
average				**4.73±0.16**	**1.03±0.04**
Hall measurement result				**4.10**	**0.91**

Table 5.1 Summary of TLM measurement of sample (a) H062 (b) H075.

We are unable to obtain accurate values for the transfer length or the specific contact resistivity for the following reasons. All these results were extracted from the line fits in Fig 5.2. However, a small error of the slope can cause a relatively large percentage error in the intercept on the distance and resistance axis, which are used to obtain the transfer length and contact resistance of the ZnO/Al contact. As a result the errors are as large as ~ 100% in some cases for the transfer length, and in one case the calculated transfer length was negative. Since the specific contact resistivity is derived from the transfer length squared (Eq. 2.14), the percentage errors are even larger and are not quoted, as the usual equations for error propagation apply to small percentage errors. The data clearly indicate that more data points and smaller contact spacings are necessary to improve the measurement accuracy of the transfer length and contact resistivity. Nevertheless, we can say from these data that the specific contact resistivities are on the order of less than 10^{-4} Ω cm^2 for the best case devices. In addition, the specific contact resistances of the two step sample (H075) appear to be lower than those of the single step sample (H062). A contact resistivity of 10^{-5} $\Omega \cdot cm^2$, is considered good Ohmic behaviour for many devices. [54]

In summary, from the TLM data, we have confirmed that Al is a good metal for making Ohmic contacts on MOCVD-grown ZnO. The resistivity of the ZnO film from the TLM measurements agreed very well with the Hall data and the specific contact resistance was low. There are still some improvements that need to be implemented in future work. The relatively large errors for contact resistance can be reduced by increasing the number of data points on the distance versus resistance figure. The size and spacing of the metal pads on the mask should be shrunk to increase the precision of this measurement.

5.2 Rectifying Au contacts for ZnO on Si substrates

The comparison of material quality of ZnO on Si (111) and sapphire (001) substrates was presented in Chapter 4. In this section, the current voltage characteristics of rectifying Au contacts on ZnO grown on Si (111) substrates are presented. ZnO on Si (111) was chosen because of the ease of contacting the backside through the heavily doped *n*-type Si substrate. However, as discussed in Chapter 4, the material quality of growth on Si(111) is greatly inferior to films grown on sapphire.

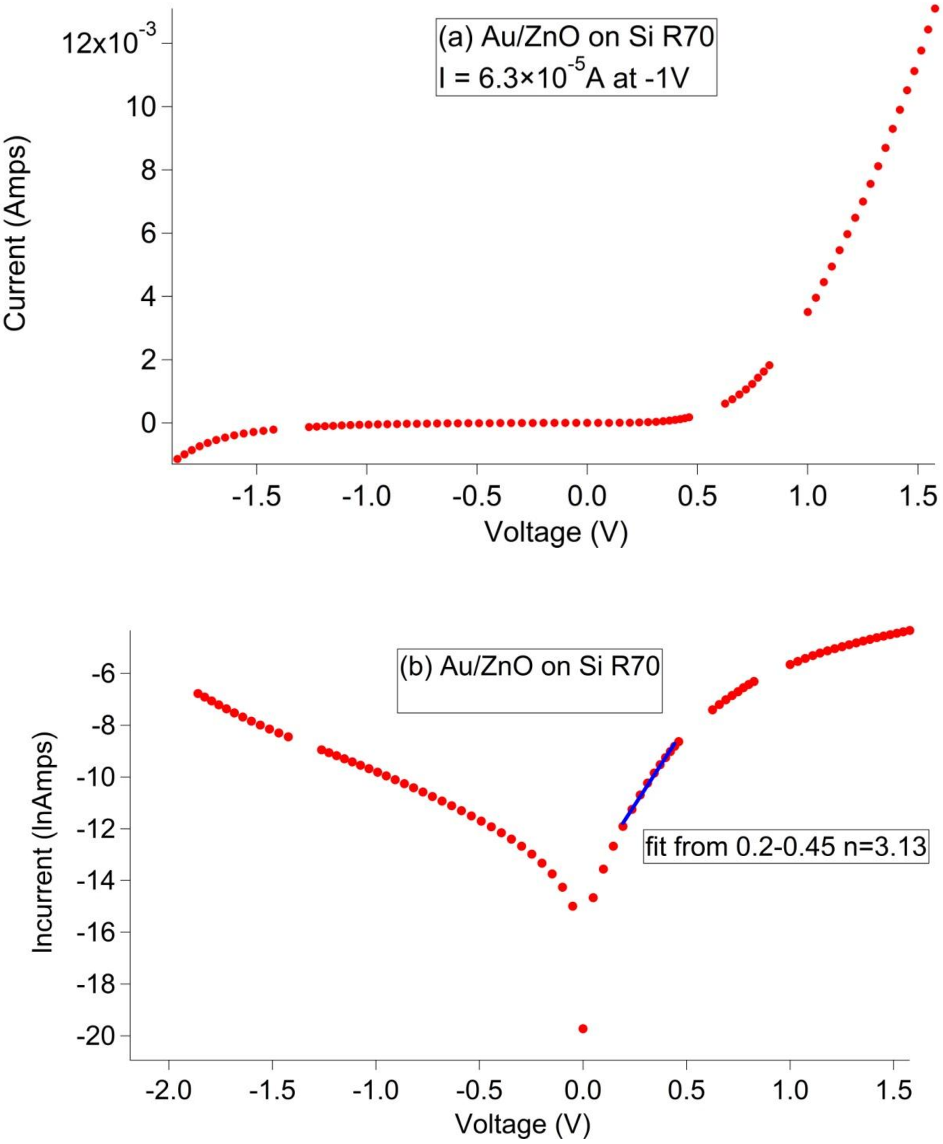

Figure 5.3 The current-voltage characteristics of the Au/ZnO contacts on *n*-Si substrate on (a) linear scale (b) log scale.

ZnO/Si wafer R70 was first cleaned with acetone, isopropanol and water before deposition, each step lasting for 5 minutes. 100 nm thick Au circles with 250 µm diameter were then deposited by thermal evaporation on the surface of the ZnO through a shadow mask to fabricate rectifying contacts. A layer of indium was coated on a piece of copper sheet which had been cleaned in a mixture of HCl and DI water (1:20 ratio) and then the copper sheet was connected with the backside of the ZnO device to form the back contact electrode for the *I-V* measurements.

Fig 5.3 shows the current-voltage curves of sample R70, both on a log and linear scale. The linear scale *I-V* curve shows rectifying characteristics with a reverse leakage current density of about 10^{-2}A/cm^2 at -1V. Compared with literature values for ZnO substrate material, [16] the leakage current is still very large, which may be due to the high carrier concentration in the surface region of the ZnO.

Thermionic emission (TE) theory predicts that the current-voltage characteristic with the series resistance is given as follows: [3]

$$I = I_0\left[exp\left(\frac{q(V-IR_S)}{nkT}\right)-1\right] \tag{5.1}$$

where n is unity for an ideal diode. For these devices, the ideality factor n was 3.19 based on a fit from 0.2V to 0.45V, which was higher compared with rectifying Au contacts on ZnO thin film on Si substrate reported in the literature. [56] Such high values of n can be attributed to the prevalence of tunnelling in the surface region [57] especially considering the high electron concentrations obtained from *C-V* measurements (to be discussed later). The existence of an interfacial layer and/or interface states or surface roughness might be other reasons causing such a high ideality factor. [46]

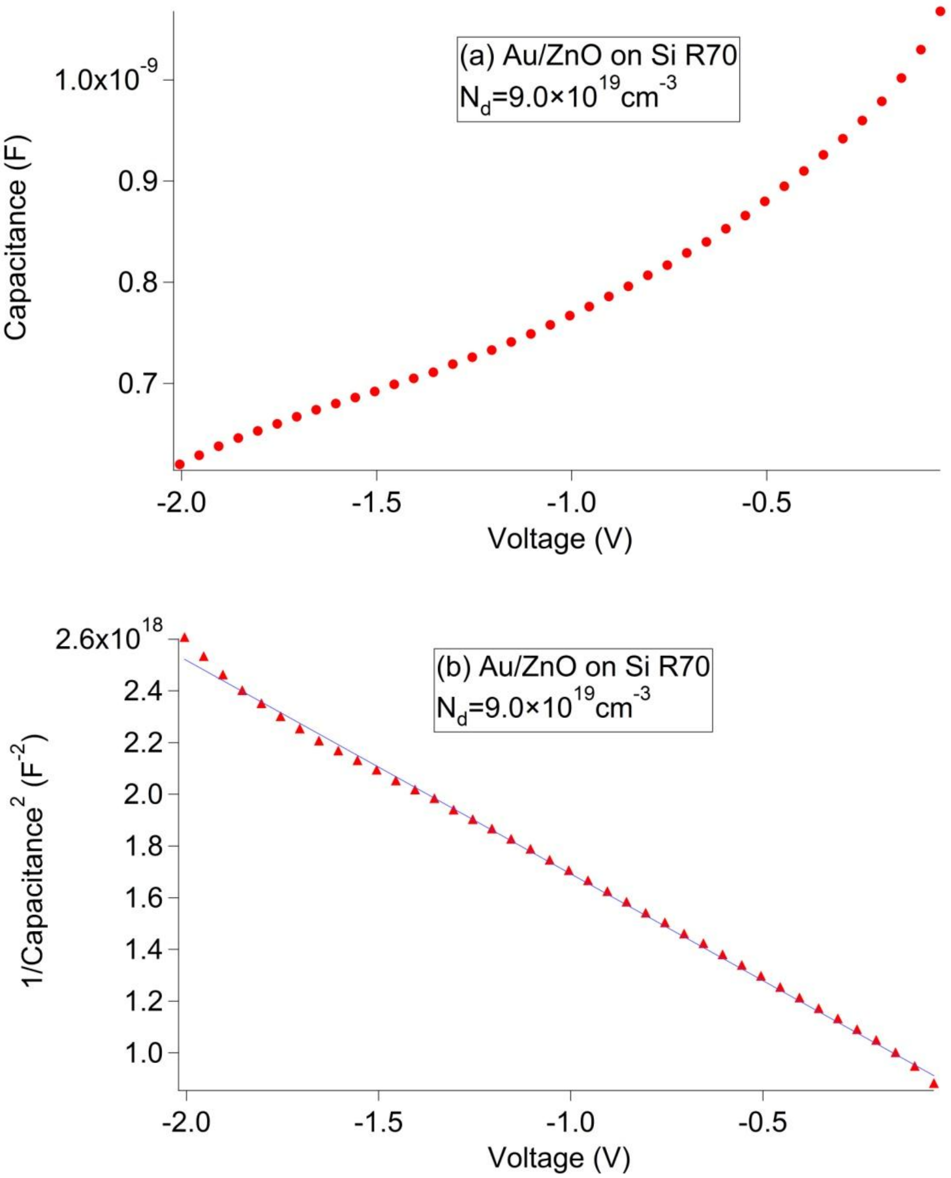

Figure 5.4 The reverse-bias (a) C-V and (b) $1/C^2$ vs. V plots for Au/ZnO rectifying contacts on sapphire substrates.

The C-V curve for the ZnO/Si sample is shown in Fig 5.4. These data provide estimates of the barrier height and carrier concentration. The C-V results indicate a very high donor concentration of $9.0 \times 10^{19} cm^{-3}$ which is much higher than the electron concentration observed by Hall or the donor concentration observed by C-V measurements for samples grown on sapphire. This may due to the polycrystalline nature of ZnO on Si substrates which we have discussed in Chapter 4. The built-in potential can be extracted from the intercept of the $1/C^2$-V curve, and is about 1.65V. This value is also higher compared with results from the literature. [58]

5.3 Rectifying Au contacts for ZnO on sapphire substrates

We could not follow the same backside contact procedure to fabricate rectifying contacts for ZnO on sapphire substrates because the sapphire is such a good insulator. To solve this problem, both rectifying and Ohmic contacts were deposited on the top side of the ZnO thin films. The experimental procedure was discussed in Chapter 3. Al was deposited on the surface of ZnO as the Ohmic contact and then Au was deposited on circular patterned areas with a small gap of 10 µm between the Au and the Al. Four different rectifying contact areas were used for comparison. Some of these samples have been treated with oxygen plasma or hydrogen peroxide to improve the rectifying behaviour, which will be discussed in the next section. Then *I-V* and *C-V* measurements were carried out. In this section, the *I-V* and *C-V* results of as-received samples will be discussed. A qualitative model of current transfer through the junctions will be provided and the effect of surface treatment for the rectifying Au contacts will be presented.

5.3.1 Rectifying Au contacts on as-received samples

To investigate the reproducibility of the rectifying Au contact results, the device was divided into 9 areas, each group containing all 4 different size rectifying contacts: 50 µm, 100 µm, 250 µm, 500 µm. *I-V* and *C-V* measurements were carried out and compared for diodes within the same area or among different areas.

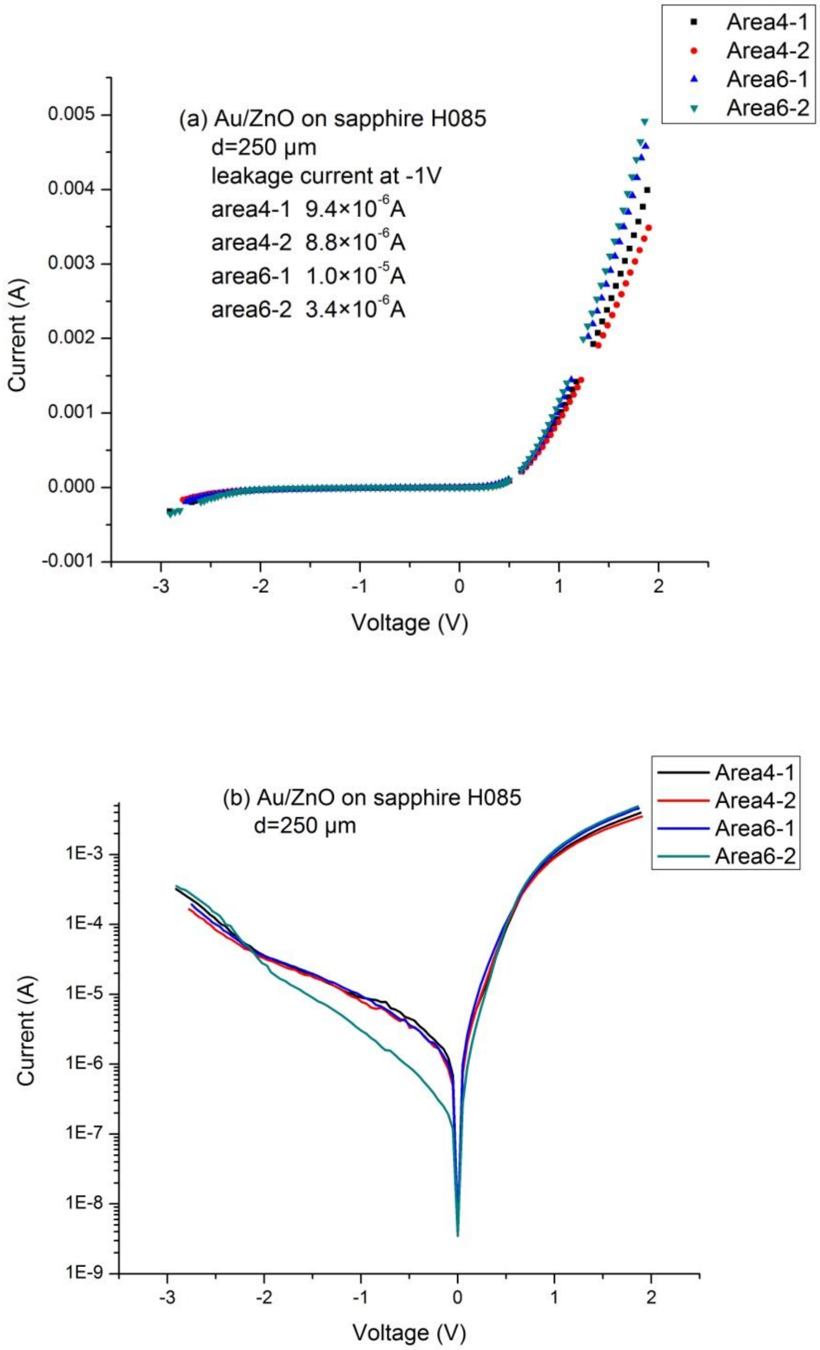

Figure 5.5 *I-V* characteristics for Au-ZnO devices on sapphire, sample H085 (a) linear (b) log scale.

Fig 5.5 shows *I-V* measurements of Au-ZnO diodes with 250 µm diameter contacts. Devices from area 4 and area 6 are shown for comparison. It can be seen that all the *I-V* curves are similar with the exception of a higher leakage current for device 6-2. These curves clearly show rectifying behaviour with reverse currents density at -1V of $10^{-1}{\sim}10^{-2}$ A/cm^2 which is still large compared with some literature values. [59] For the curves shown in the graph, the ideality factors, which can be extracted from *I*-*V* curves in log scale, are 4.7, 4.0, 4.9 and 4.3. The ideality factor is much greater than one, similar to other groups' Au/ZnO devices grown by MOVPE. [50]

As mentioned before, four different sizes of contacts were fabricated for comparison. To investigate the influence of contact area, the current density was plotted as a function of voltage, as shown in Fig 5.6. Since the uniformity is good for these samples, here we just show the comparison of different adjacent contact sizes. For forward and reverse bias there is a clear increase in the current density with device diameter.

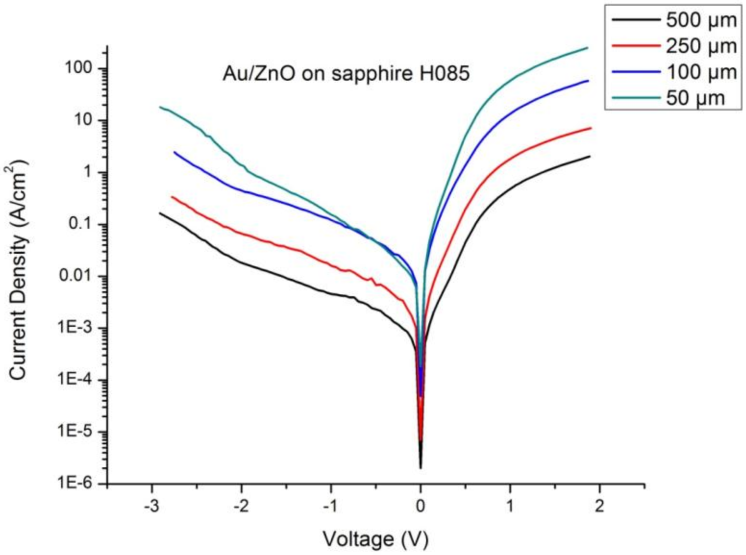

Figure 5.6 Current density vs. voltage for different diameter Au-ZnO devices on sapphire, sample H085.

The device current can be modelled as a diode resistance in series with a contact resistance and a bulk contribution from the ZnO in the gap between the Au contact and the Al electrode. The bulk contribution is due to conduction in the 10 μm thick annular cylindrical ring of ZnO between the rectifying Au contact and the Ohmic Al contact. The bulk resistance is given by $R_b \sim \rho L_g/(2\pi r t)$, where L_g=10 μm is the gap, t is the layer thickness and r is the inner contact radius. For forward bias, the bulk resistance is expected to dominate the current, which should therefore scale as r rather than as the area. In addition there should be a contribution from the contact resistance as shown in Fig 5.7. The contact resistance is given by $R_c = R_c'/(L_t \cdot 2\pi r)$ where L_t is the transfer length and $R_{c'}$ is the specific contact resistivity (Ohm·cm^2). Both the bulk and contact resistance vary as $1/r$, therefore the forward current should also vary as r.

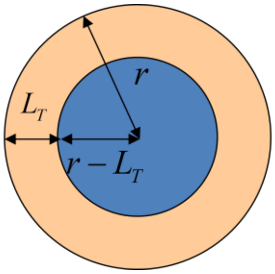

Figure 5.7 Schematic of Au--ZnO rectifying contact (top view) showing the transfer length for the forward biased Au contact. A similar annular contact region exists for the Al contact (not shown).

Figure 5.8 shows a plot of the forward current for four different device sizes at voltage of 1V. The line shows a linear fit to the data showing a clear linear trend as expected based on the previous argument.

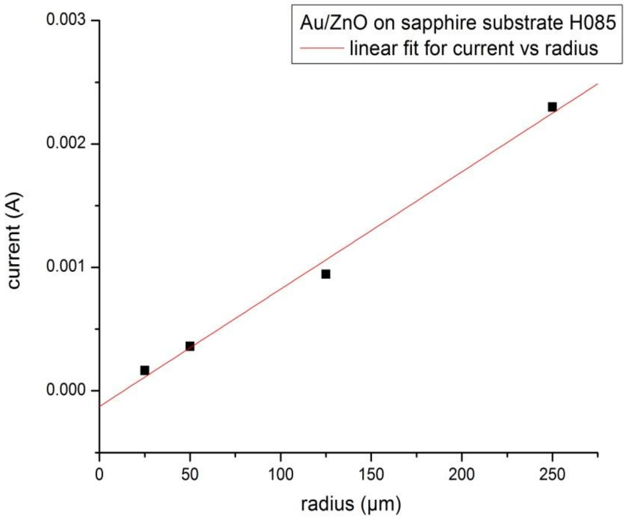

Figure 5.8 Current vs. contact radius for rectifying Au on ZnO/sapphire H085 at 1V forward bias.

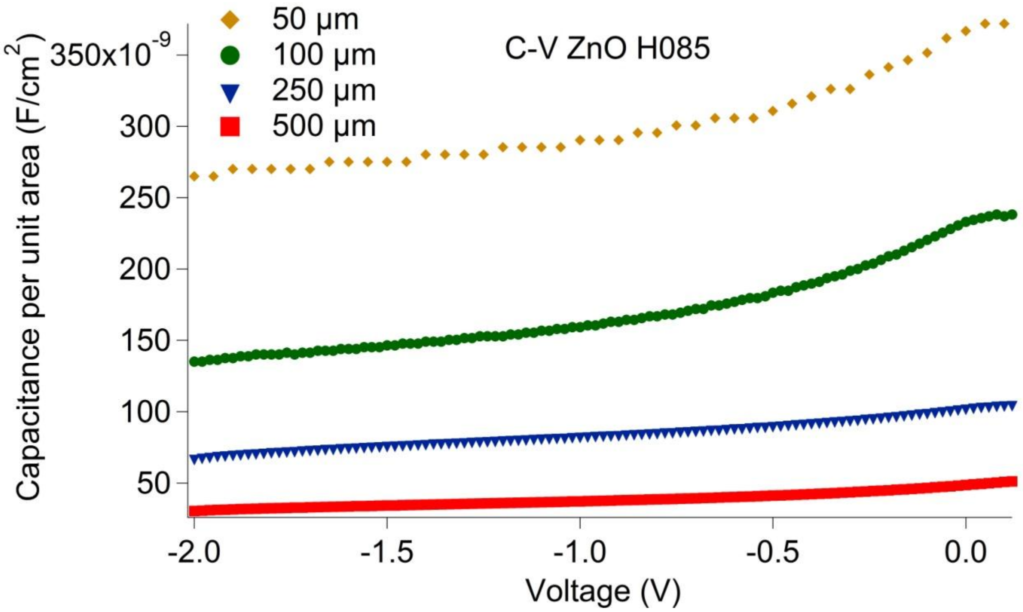

Figure 5.9 Capacitance per unit area vs. voltage for different device sizes for Au-ZnO sample H085.

The *C-V* measurements show a similar trend to the *I-V* measurements. Fig 5.9 shows a plot of the capacitance per unit area versus voltage. Ideally, the four curves representing four different contact areas should overlap with each other if the quality and properties of the diode didn't change with area. However, the *C-V* measurements show a strong size effect. To further study this issue, the capacitance versus diameter was plotted in Fig 5.10.

Fig 5.10 shows several capacitance vs. diameter curves for rectifying Au contacts at different voltages. The data show a linear increase in capacitance with diameter rather than the quadratic behaviour which would be expected for a diode with top and bottom contacts. This suggests that the depletion width is only changing in an annular region near the edge of the circular mesa rather than throughout the entire metal surface.

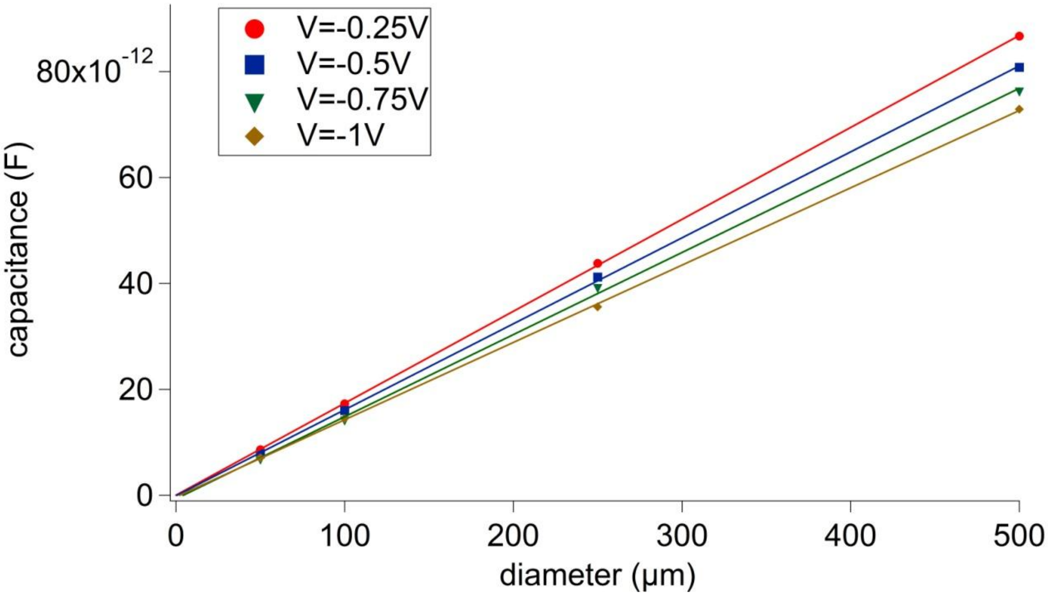

Figure 5.10 Capacitance vs. diameter for Au rectifying contacts on ZnO/sapphire H085.

The following is a qualitative explanation for this trend. The diodes are quite leaky compared with high quality diodes typically prepared on ZnO substrate material. The current flow will be primarily through an annular region of the Au electrode and the Al electrode as was the case for the TLM measurements. This means that the region closer to the center of the Au contacts will have very little current flow, with the result that the ZnO under the center region is essentially at the same potential as the Au itself. Since the sapphire is an excellent insulator, it will not facilitate the flow of current through the center region of the contact. As a result, the potential of the ZnO under the diode will tend to be the same as the potential of the Au contact, independent of the applied voltage, resulting in a constant depletion width. As a result, a *C-V* measurement will mostly be affected by changes in the charge near the edge of the Au contact.

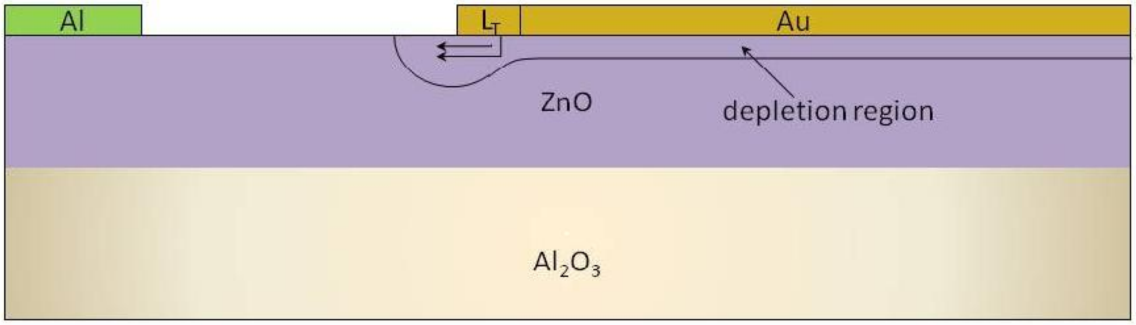

Figure 5.11 Schematic of the depletion area under the Au metal. Because of current leakage in reverse bias, only the depletion region at the edges will change with bias voltage. Arrows show primary region with current flow.

Figure 5.12 shows plots of the inverse square of capacitance per area versus voltage for the four different device sizes for sample H085. Ideally, the fits should be linear over the entire voltage range, however it is clear that this is not the case for these devices. Fit lines are shown at -1V and 0V. The carrier concentrations and built-in potentials of sample H085 calculated from *C-V* data for these two bias voltages are shown in Table 5.2. The carrier concentrations were calculated assuming the nominal Au contact area, neglecting the previously described edge effects, which could not be included quantitatively. Also shown are the leakage current densities at -1V, and the built in voltages and ideality factors obtained from the *I-V* data. Four diodes for each contact size were chosen and the average value and standard deviation was summarized in this table. The apparent concentration increased as the contact size reduced, but we believe this is an artefact due to the previously discussed edge effects. The carrier concentration obtained from Hall measurements for ZnO H085 is $1.9 \times 10^{18} cm^{-3}$, which is much closer to the 50 µm contact data at 0V. This indicates that the effective contact area is closer to the real contact area when the radius is 50 µm and confirms the above qualitative discussion of the depletion region only varying near the edge of the contact.

In general the values of the built in voltages obtained from *I-V* data are seen to compare better with the *C-V* measurements at 0V bias than -1V bias. This may be due to the larger leakage currents affecting the *C-V* measurement process at -1V. The ideality factor seems to increase as the diode size decreases. This may be due to a higher concentration of surface states near the contact edges.

Finally we complete the present analysis by estimating the depletion width for these epilayers. Based on the measured Hall concentration of 1.9×10^{18} cm^{-3} for sample H085, we estimate a zero bias voltage depletion width of 23.6 nm using equation 2.7, and assuming a dielectric constant of 7.9 and a built in voltage of 1.4V. This is much less than the nominal layer thickness of ~500 nm.

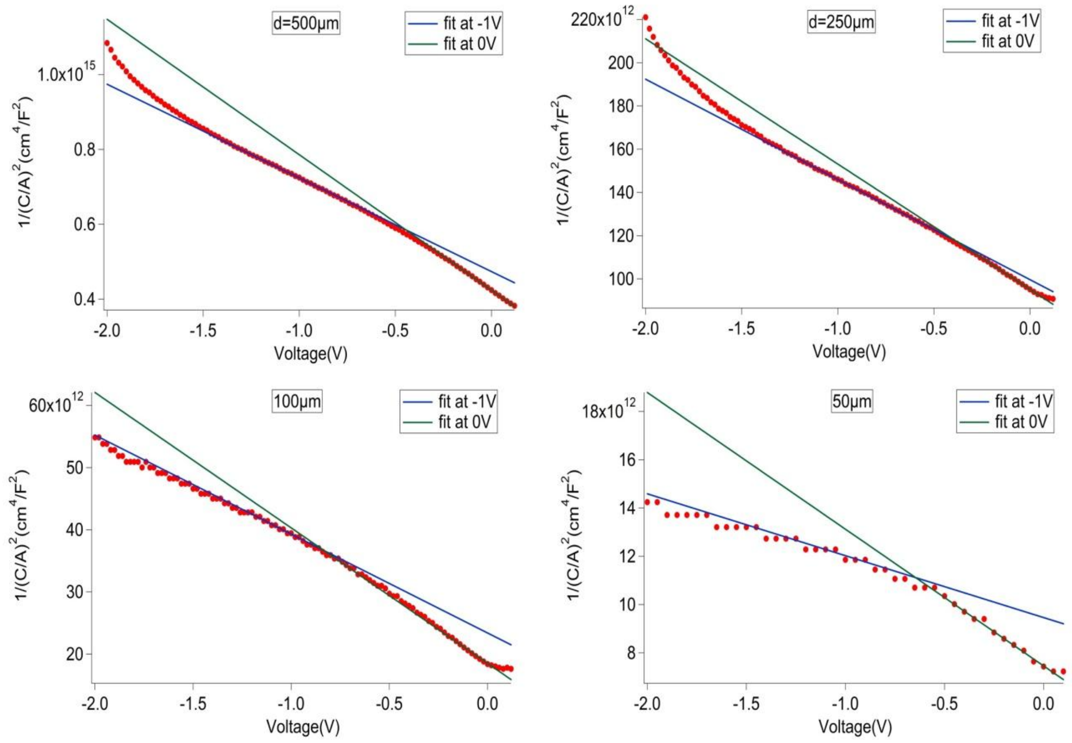

Figure 5.12 $1/(C/A)^2$ vs. V plot for Au rectifying contacts on ZnO/sapphire H085. Fits are shown at -1V and at 0V.

Device Diameter (μm)	J at -1V (A/cm^2)	N(cm^{-3}) (@-1V)	V_{bi}(V) (@-1V)	N(cm^{-3}) (@0V)	V_{bi}(V) (@0V)	ϕ_{B0}(V) (from *I-V*)	Ideality factor (from *I-V*)
500	0.023±0.01	7.1×10^{16}	1.89	4.9×10^{16}	1.17	1.44	4.1±0.1
250	0.0016±0.005	3.7×10^{17}	2.15	3.1×10^{17}	1.64	1.34	4.5±0.3
100	0.035±0.01	1.1×10^{18}	1.47	8.2×10^{17}	0.84	1.39	5.0±0.4
50	0.13±0.05	7.0×10^{18}	3.69	3.0×10^{18}	1.31	1.40	6.0±0.5

Table 5.2 Summary of properties of Au rectifying contacts on ZnO/sapphire (sample H085).

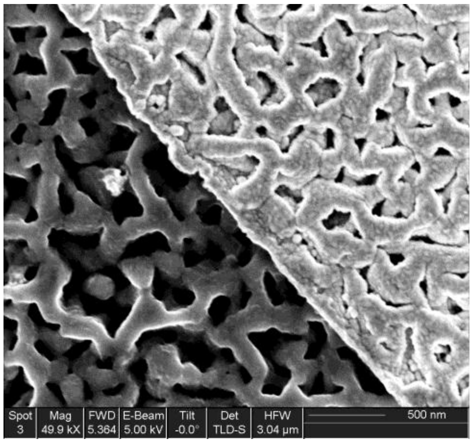

Figure 5.13 Scanning electron micrograph of a gold contact (upper right) on the ZnO H085 epilayer (lower left). Image courtesy of Thomas Wintschel.

Figure 5.13 shows a scanning electron micrograph of the actual morphology of our device layers. The image shows that the actual microstructure is quite porous and contains many voids. Clearly many of the assumptions used in the above analysis will break down for such a film.

5.3.2 Surface treatment for ZnO/sapphire rectifying contacts

Surface treatments such as oxygen plasma exposure and hydrogen peroxide solutions were reported to improve the properties of ZnO rectifying diodes. [60] Oxygen plasma treatment was reported to be a good method to remove surface OH conduction layers in order to decrease the surface conductivity. [49] The adsorbed oxygen species can diffuse into the lattice and act as electron acceptors, which will also lower the surface conductivity. This process was critical for diode barrier formation. [49] In this part of the thesis, we investigate the effects of oxygen plasma and hydrogen peroxide treatment on the properties of our Au-ZnO diodes grown by MOCVD. The device fabrication procedure was the same as before but the device was exposed to 30W, 0.050Torr oxygen plasma for 2.5 minutes after the Al contact was deposited on the ZnO film. Then Au was deposited on the patterned area to form a rectifying contact. Fig 5.14 shows the comparison of the *I-V* curves for Au-ZnO devices with and without the plasma treatment. The same data are plotted on a log scale for comparison in Fig 5.15 and the results of the *I-V* measurements are summarized in Table 5.3. From the results of Fig 5.14, we can see that for all four contact sizes, the plasma treatment increases the forward current somewhat. Table 5.4 compares the series resistance for plasma treated samples and as-received samples, and it is clear that the plasma treatment does reduce the resistance. As before, the series resistance was proportional to r, not r^2 confirming that the effective area was the ring area, not the whole contact area. Also, there seems to be no significant improvement of the leakage current. From Table 5.4, the ideality factor improved somewhat after the plasma treatment. The leakage current at -1V and the carrier concentration didn't show much difference and the built-in potential barrier increased after the treatment.

C-V measurements were also performed on this set of samples and the results were similar in form to those on the untreated ZnO samples. Carrier concentrations and built-in voltages were estimated from fits to the $1/(C/A)^2$ vs. V data averaged over the voltage range from -1 to 0V. The results are summarized in Table 5.3. The apparent carrier concentration was observed to decrease significantly compared with the untreated samples. Again, we get better agreement with the Hall data for the 50 µm devices. For example, the *C-V* data for the 50 µm plasma treated device indicates N_d=2.3×10^{18} cm^{-3} compared with the measured Hall value of 2×10^{18} cm^{-3}.

	Diameter (μm)	N (10^{17}cm-3)	V_{bi}(V) from CV	ϕ_{B0} (V) from IV	Ideality factor	current at -1V(A)
Plasma treated	500	2.15	2.05	1.44	2.92	2.2×10^{-5}
	250	3.90	1.15	1.35	3.20	1.0×10^{-5}
	100	9.81	0.98	1.40	3.25	2.6×10^{-6}
	50	22.8	1.39	1.42	3.00	5.3×10^{-7}
As received	500	1.49	1.17	1.44	3.71	3.7×10^{-5}
	250	4.87	1.64	1.34	4.16	1.2×10^{-5}
	100	8.99	0.84	1.39	4.56	1.6×10^{-6}
	50	50.9	1.31	1.40	5.37	1.8×10^{-6}

Table 5.3 Summary of comparison of plasma treatment for Au contacts on ZnO H085.

Diameter (μm)	R_s as received (ohm)	R_s plasma treated (ohm)
500	92	80
250	199	182
100	450	427
50	1126	833

Table 5.4 Series resistance of Au contacts on ZnO H085 for as-received sample and plasma treated sample.

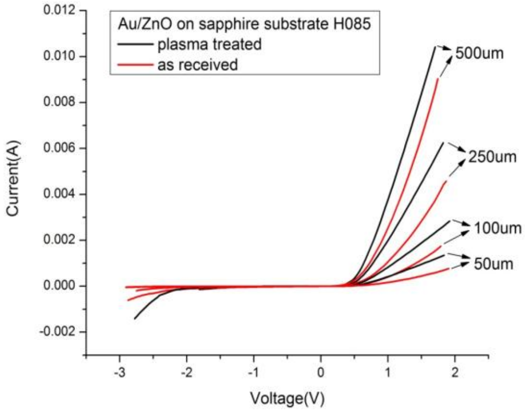

Figure 5.14 Comparison of *I-V* curves of plasma treated and as-received devices for Au rectifying contacts on ZnO H085 (linear scale).

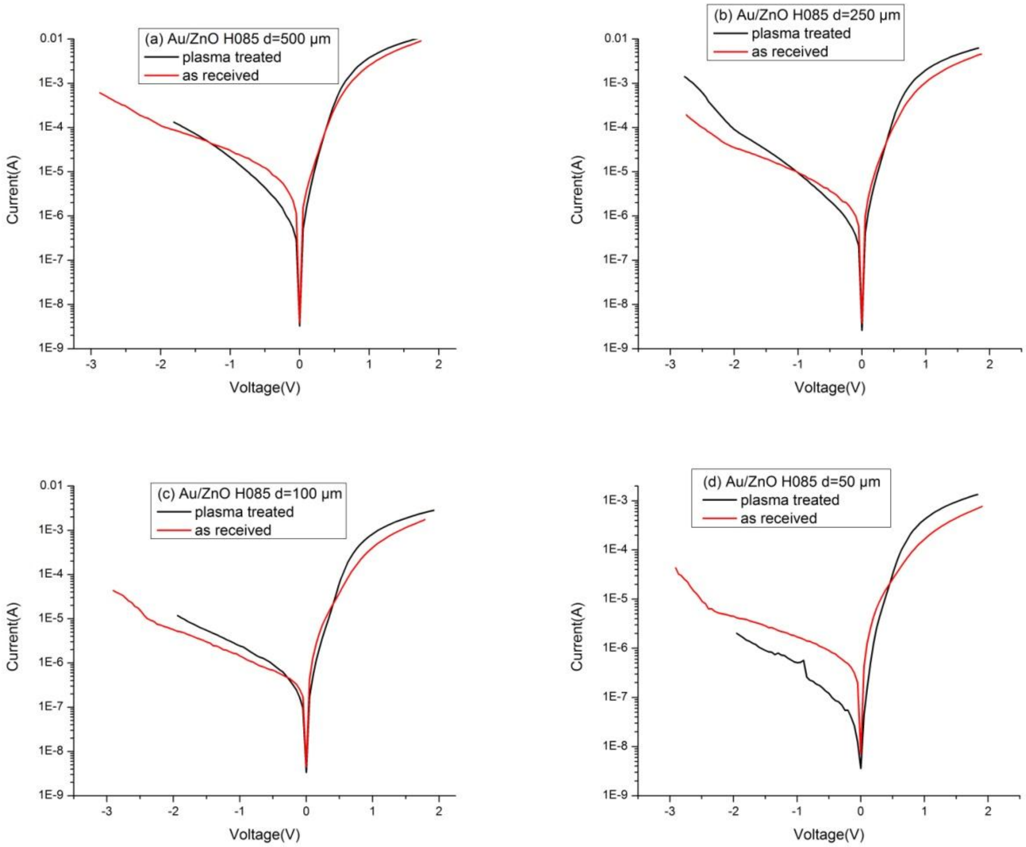

Figure 5.15 Comparison of plasma treated devices with Au rectifying contacts on ZnO H085 (log scale).

Hydrogen peroxide treatment is another method which is reported to improve the quality of rectifying metal-ZnO diodes. [50] Hydrogen peroxide treatment is expected to remove the surface OH layer, similar to the plasma treatment. According to some works, [61] the OH layer on the top surface may result in a heavy-doped *n*-type surface layer, making the junction behave like an Ohmic contact. Hydrogen peroxide treatment is expected to remove this OH layer through the reaction of deep level defects with the oxygen radicals supplied by the dissociation of hydrogen peroxide, filling oxygen vacancies, and forming ZnO. [61] The space charge region is wider after the hydrogen peroxide treatment, which will force the electrons to climb over the barrier near the interface instead of tunnelling through the barrier. Hence, the *I-V* characterization will mainly be determined by the thermal emission process.

In our case, Al was first deposited on the surface of the ZnO as usual. A layer of photoresist was then coated on top of the Al layer. This layer of photoresist was used to pattern a particular area for Au deposition. Also, it protects the Al layer from being oxidized. The device was then placed into 30°C hydrogen peroxide for 10 minutes. After the treatment, then the Au was deposited. The *I-V* data is shown in Fig 5.16.

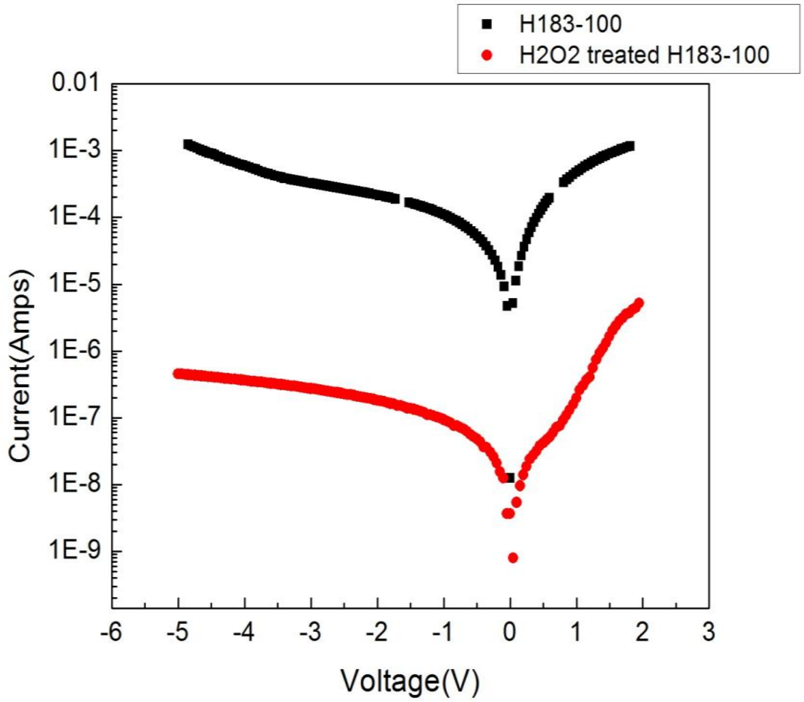

Figure 5.16 Comparison of *I-V* curves for hydrogen peroxide treated and as-received Au contacts (100 µm Au) on ZnO/sapphire (sample H183).

Fig. 5.16 clearly indicates that the hydrogen peroxide does improve the quality of the rectifying Au contacts by increasing the forward-to-reverse current ratio, but at the same time, the diode series resistance was increased dramatically by a factor of ~10^3. Due to the high resistance, *C-V* measurements could not be carried out. Hence we just show the built-in barrier heights extracted from the *I-V* measurements. The results are shown in Table 5.5.

	Diameter (μm)	**ϕ_{B0}(V) from IV**	**Ideality factor**	**current at -1V(A)**	**Series resistance(ohm)**
H_2O_2 treated	500	0.63	4.44	1.0×10^{-7}	2.3×10^{4}
	250	0.61	4.89	9.6×10^{-8}	4.9×10^{4}
	100	0.62	4.56	9.4×10^{-8}	1.2×10^{5}
As received	500	0.42	4.55	1.1×10^{-3}	55.4
	250	0.42	4.15	4.8×10^{-4}	131
	100	0.43	4.09	1.1×10^{-4}	300

Table 5.5 Summary of comparison of H_2O_2 treatment for Au rectifying contacts on ZnO (sample H183).

From Table 5.5, there is no significant improvement of ideality factor for the hydrogen peroxide treated samples. Such a high ideality factor can be attributed to the existence of interfacial layers or surface states. [46] Similar to other group's results [62], the hydrogen peroxide treatment significantly increased the series resistance by a large factor.

To summarize this chapter, TLM results showed that Al was a good metal for making Ohmic contacts to MOCVD ZnO. Rectifying *I-V* characteristics were observed for Au contacts on ZnO both grown on Si and Al_2O_3 substrates, but they showed large leakage currents and high ideality factors. Also, an interesting size dependence effect was found for both *I-V* and *C-V* data. The forward current was found to depend on r instead of r^2 and this was shown to be a result of the specific way top side contacts were applied. The capacitance also depended on the radius rather than the area and this was postulated to be due to the high leakage of our diodes, resulting in a depletion width that changed with bias only near the contact edges. Capacitance-voltage measurements at zero bias gave carrier concentrations that agreed reasonably well with Hall measurements for the smallest contact areas. Surface treatments were performed to try to improve the properties of Au-rectifying contacts, however, both oxygen plasma treatment and hydrogen peroxide treatment did not show significant improvements.

6: CONCLUSIONS AND FUTURE WORK

This thesis explored the electrical properties of MOCVD-grown ZnO thin films by various electrical characterization techniques including Hall effect, TLM, *I-V*, and *C-V* measurements. Intentional doping with substitutional donors like Al and In was not found to be very effective despite evidence from PL and SIMS measurements of large amounts of donor incorporation. This discrepancy may be due to the poor crystal quality of our films which results in large densities of native defects and grain boundaries which dominate the electrical resistance of the layers. While rectifying diodes were achieved using Au contacts, the properties were poor in comparison with devices reported in the literature which were usually grown on high quality bulk ZnO substrates. Several things should be done in the future to improve the performance of the rectifying contacts:

- The MOCVD ZnO material which was used to fabricate Au-ZnO devices was not optimal. The electron concentration from Hall measurements was about 10^{18} cm^{-3} which is very high. High concentrations can increase the leakage current of the Au-ZnO contacts. In the future, Au contact devices on better quality ZnO should be fabricated for *I-V* characterization. This is now possible using recent epilayers with greatly reduced free carrier concentrations.
- The surface morphologies of the films used in this study have recently been investigated in detail using SEM and it was found that in many cases the films consist of high densities of nanorods and void regions. This is clearly not optimal for the formation of planar devices. The use of alternate orientation sapphire substrates may

permit higher quality 2-d growth. Growth on ZnO substrates should also be considered. This has been reported to permit atomically smooth films. Recent work in our lab has shown that the films can be greatly smoothed using In doping. Rectifying Au-ZnO devices should be grown on low-doped layers grown on In-doped buffer layers.

- Other kinds of metals such as Pt and Pd which are also expected to form good rectifying contacts on ZnO can also be tried.
- A highly conductive ZnO layer can be deposited on the sapphire first, followed by epitaxial growth of a lower-doped ZnO film. This highly conductive ZnO layer can force the current to flow vertically through the film rather than laterally as is the present case with Al ring contacts.

APPENDIX

Summary of growth conditions and Hall measurements for samples processed into Au-ZnO diodes.

Sample Number	Growth Temperature	Growth condition	Resistivity (ohm·cm)	Carrier Concentration (cm^{-3})	Mobility (cm^2/Vs)	Hall ratio
H062	800	40sccm DEZn, 4SLM N2O, 60mins				
H075	500/800	40sccm DEZn, 2SLM N2O, 500C+5mins and 800C+40 mins	4.10E-02	3.20E+18	47.55	1.02
H085	500/800	40sccm DEZn, 2SLM N2O, 500C+20mins and 800C+40 mins	5.36E-01	1.87E+18	6.23	1.15
H233	800	2.0sccm DMZn, 3slm N2O,60min	5.13E-1	2.20E17	60	1.05
H266	800	TMIn 1sccm, no substrate clean or anneal sccm 2.0 sccm DMZn, 3.0 slm N2O, 60min	5.78	9.84E+16	11.01	1.03
H282	800	undoped, 2.0 sccm DMZn, 3 slm N2O, 60 min, cleaned and annealed substrate	2.08	8.29E+16	36.14	1.11
H285	800	5.0 sccm TMIn, 2.0 sccm DMZn, 3 slm N2O, 60 min, cleaned and annealed substrate	2.84	7.29E16	30.12	1.06

BIBLIOGRAPHY

1. V.A.Coleman *et.al* in *Zinc Oxide Bulk, Thin Film and Nanostructures*, Chapter 1, Basic Properties and Applications of ZnO, Ed. by C. Jagadish and S Pearton, Elsevior, 2006.
2. Ü. Özgür,Y. I. Alivov, C. Liu, A. Teke, M.A. Reshchikov, S. Doğan, V. Avrutin, S.J. Cho, H. Morkoç, J. Appl. Phys., **98**, 041301 (2005)
3. D.A.Neaman, *Semiconductor Physics and Devices: Basic Principle*. McGraw-Hill Press, Third Edition, 2003.
4. B.G.Streetman. *Solid State Electronic Devices*. Prentice-Hall Press, Second Edition, 1980.
5. D.K.Schroder. *Semiconductor Material and Device Characterization*. John Wiley & Sons Ltd, Third Edition, 2006.
6. D.P.Kennedy and P.C.Murley, IBM J. Res. Dev., **12,** 242 (1968)
7. H.Murrmann and D.Widmann, IEEE Trans.Electron.Dev. ED-16, 1022 (1969)
8. H.H.Berger, Solid-State Electron., **15**,145 (1972); H.H.Berger, J. Electrochem. Soc., **119**, 507 (1972)
9. Van der Pauw, L.J, Philips. Res. Reports., **13**, 1 (1958)
10. D.C.Look., *Methods in Materials Research*, Wiley, New York, 2000.
11. Hadis Morkoc, *Handbook of Nitride Semiconductors and Devices* 2008.
12. Richard C.Jaeger, *Introduction to Microelectronic Fabrication*, Second Edition, Prentice Hall Press, 2002

13. S.H.Nam, M.H.Kim, D.G.Yoo, S.H.Jeong, D.Y.Kim, N.E.Lee and J.H.Boo, Surf. Rev. Lett., **17**, 121 (2010)
14. W.R.Liu, Y.H.Li, W.F.Hsieh, C.H.Hsu, W.C.Lee, M.Hong, J.Kwo, J. Phys. D 41, 065105 (2008)
15. J.Y.Shi, L.P.Yu, Y.Z.Wang, G.Y.Zhang and H.Zhang, Appl. Phys. Lett., **80**, 2293 (2002)
16. S.P.Watkins, Z.W.Deng, D.C.Li and H.Huang, submitted for J. Appl. Phys (2011)
17. H.Huang, S.P.Watkins, unpublished work
18. I.Ohkubo, Y.Matsumoto, A.Ohtomo, T.Ohnishi, A.Tsukazaki, M.Lippmaa, H.Koinuma, M.Kawasaki, Appl. Surf. Sci., **159**, 514 (2000)
19. Y.F.Chen, D.M.Bagnall, H.J.Koh, K.T.Park, K.J.Hiraga, Z.Q.Zhu and T.Yao, J. Appl. Phys., **84**, 3912 (1998)
20. T. Moriyama, S. Fujita, J. Cryst. Growth., **298**, 464 (2007)
21. W. Guo, A. Allenic, Y.B. Chen, Z.Q. Pan, W. Tian, C. Adamo, D.G. Schlom, Appl. Phys. Lett., **92**, 072101 (2008)
22. J.Y. Park, D.J. Lee, B.T. Lee, J.H. Moon, S.S. Kim, J. Cryst. Growth., **276**, 165 (2005)
23. D.C.Look *et.al* in *Zinc Oxide Bulk, Thin Film and Nanostructures*, Chapter 2, Doping and Defects in ZnO, Chennupati Jagadish and Stephen Pearton, Elsevior, 2006.
24. C.G.Van de Walle, Phys. Rev. Lett., **85**, 1012 (2000)
25. S.Y.Myong, S.J.Baik, C.H.Lee, W.Y.Cho and K.S.Lim, Jpn.J. Appl. Phys., Part 2 **36** L1078 (1995)

26. H.J.Ko, Y.F.Chen, S.K.Hong, H.Wenisch, T.Tao and D.C.Look, Appl. Phys. Lett., **77** 3761 (2000)
27. H.Huang, summary for private communication.
28. K.S. Weisenrieder, J.Müller, Thin Solid Films., **300**, 30 (1997)
29. Thomas Wintchel, private communiation.
30. Performed by Evans Analytical Group.
31. Tammy Ben-Yaacov, Tommy Lve, Chris G.Van de Walle, Umesh K. Mishra, James S. Speck and Steven P. Denbaars Phys.Status.Solidi **C6**, 1464 (2009)
32. J.C.Sun, T.P.Yang, G.T.Du, H.W.Liang, J.M.Bian and L.Z.Hu, Appl. Surf. Sci., **253**, 2066 (2006)
33. J.D.Albrecht, P.P.Ruden, S.Limpijumnong, W.R.L.Lambrecht and K.F.Brennan, J. Appl. Phys., **86**,6864 (1991)
34. B.K.Meyer, H.Alves, D.M.Hofmann, W.Kriegseis, D.Forster, F.Bertram, J.Christen, A. Ho_mann, M.Straburg, M.Dworzak, U.Haboeck, and A.V.Rodina, Phys. Stat. Sol. (b), **241**, 231 (2004)
35. D.C.Look, H.L.Mosbacker, Y.M.Strzhemechny and L.J.Brillson, Supperlattice. Microst., **38**, 406 (2005)
36. D.C.Look, J. Appl. Phys., **104**, 063728 (2008)
37. K.T.Roro, G.H.Kassier, J.K.Dangbegnon, S.Sivaraya, J.E.Westraadt, J.H.Neethling, A.WR.Leitch and J.R.Botha, Semicond. Sci. Technol., **23**, 055021 (2008)
38. H.Wenckstern, M.Brandt, G.Zimmermann, J.Lenzner, H.Hochmuth, M.Lorenz, and M.Grundmann, Mater. Res. Soc. Symp. Proc., **957**, 2 (2007)

39. L.Li, C.X.Shan, S.P.Wang, B.H.Li, J.Y.Zhang, B.Yao, D.Z.Shen, X.W.Fan and Y.M.Lu, J. Phys. D:Appl Phus., **42** 195403 (2009)
40. G.E.Stillman and C.M.Wolfe, Thin. Solid. Films., **31**, 69 (1976)
41. A.Y.Polyakov, N.B.Smirnov, E.A.Kozhukhova, V.I.Vdodin, K.Ip, Y.W.Heo, D.P.Norton and S.J.Pearton, Appl. Phys. Lett., **83**, 1575 (2003)
42. R.C.Neville and C.A.Mead, J. Appl. Phys., **41**, 3795 (1970)
43. N.Ohashi, J.Tanaka, T.Ohgaki, H.Haneda, M.Ozawa and T.Tsurumi, J. Mater. Res., **17**, 1529 (2002)
44. F.D.Auret, S.A.Goodman, M.Hayers, M.J.Legodi, H.A.van Laarhoven and D.C.Look, Appl. Phys. Lett., **79**, 3074 (2001)
45. S.Liang, H.Sheng, Y.Liu, Z.Huo, Y.Lu and H.Shen, J. Cryst. Growth., **225**, 110 (2001)
46. H.Sheng, S.Muthukumar, N.W.Emanetoglu and Y.Lu, Appl. Phys. Lett., **80**, 2132 (2002)
47. S.V.Slobodchikov, Kh.M.Salikhov, E.V.Russu and Yu.G.Malinin, Semiconductors, **35**, 464 (2001)
48. S.H.Kim, H.K.Kim and T.Y.Seong, Appl. Phys. Lett., **86**, 112101 (2005)
49. B.J.Koppa, R.F.Davis and R.J.Nemanich, Appl. Phys. Lett., **82**, 400 (2003)
50. Q.L.Gu, C.K.Cheung, C.C.Ling, A.M.C.Ng, A.B.Djurisic, L.W.Lu, X.D.Chen, S.Fung, C.D.Beling and H.C.Ong, J. Appl. Phys., **103** 093706 (2008)
51. A.Y.Polyakov, N.B.Smirnov, E.A.Kozhukhova, V.I.Vdodin, K.Ip, D.P.Norton and S.J.Pearton, J. Vac. Sci. Technol., **A21**, 1603 (2003)
52. J.M.Lee, K.K.Kim, S.J.Park and W.K.Choi, Appl. Phys. Lett., **78** 3842 (2001)

53. H.K.Kim, S.H.Han, T.Y.Seong and W.K.Choi, Appl. Phys. Lett., **77**, 1647 (2000)
54. H.K.Kim, K.K.Kim, S.J.Patk, T.Y.Seong and I.Adesida, J. Appl. Phys., **94**, 4225 (2003)
55. H.K.Kim, J.M.Lee, Supperlattice. Microst., **42**, 55 (2007)
56. Ş.Aydoğan, K.Çınar, H.Asıl, C.Coşkun and A.Türüt, J. Alloy. Compd., **476**, 913, (2009)
57. S.M.Sze, Physics of Semiconductor Devices (Wiley, New York, 1981)
58. G.Yuan, Z.Ye, L.Zhu, J.Huang, Q.Qian and B. Zhao, J. Cryst. Growth., **268**, 169 (2004)
59. Dhananjay, J.Nagaraju, S.B.Krupanidhi, Physics:B., **391**, 344 (2007)
60. Basavaraj Angadi, H.C.Park, H.W.Choi, J.W.Choi and W.K.Choi, J. Phys. D:Appl. Phys., **40**, 1422 (2007)
61. C.S.Singh, G.Agarwal, G.Durga Rao, Sujeet Chaudhary, R.Singh, Mat. Sci. Semicon. Proc., **14**, 1 (2011)
62. A.E.Rakhshani, Semicond. Sci. Technol., **23**, 075037 (2003)